

**POLITECNICO DI TORINO**

**Master's Degree in Mechanical Engineering**



**Master's Degree Thesis**

**Influence of Component Contact  
Interactions on the Dynamic  
Behaviour of an Aerodynamic Test Rig**

**Supervisor**

Prof. Daniela Anna Misul

**Student**

Gabriele Ronchegalli

A.y. 24/25

*I would like to dedicate this thesis to my loving parents*

## **Abstract**

This thesis presents a comprehensive modal analysis of the new test section for the acoustic wind tunnel at the Department of Turbomachinery and Fluid Dynamics, University of Hannover. The study aims to evaluate the impact of contact modifications between key components on the overall dynamic behaviour of the system. Using ANSYS and the Finite Element Method (FEM), several progressively complex models were developed, beginning with a simplified representation of the substructures and culminating in a fully detailed model that integrates all modifications.

The analysis reveals that, while the overall system exhibits high stiffness, only a limited number of vibration modes are noticeably affected by the modifications. These findings suggest that the inherent rigidity of the contact surfaces and the supporting structure largely governs the dynamic response of the system, masking the potential effects of reducing contact surfaces.

The work provides valuable insights into the importance of precise contact modelling for accurate dynamic predictions. Recommendations for future research include experimental validation to further refine and to optimize the design of the wind tunnel test section.

# Contents

<b>List of Figures</b>	<b>vi</b>
<b>List of Tables</b>	<b>viii</b>
<b>1 Introduction</b>	<b>1</b>
1.0.1 Modal Analysis . . . . .	2
1.1 The Finite Element Method . . . . .	4
1.2 Aeroacoustic Wind Tunnel . . . . .	8
1.2.1 Test section . . . . .	10
<b>2 Models</b>	<b>13</b>
2.1 Basic models . . . . .	13
2.1.1 Central mass . . . . .	14
2.1.2 Split mass . . . . .	15
2.1.3 Split mass with bonded contact . . . . .	15
2.1.4 Split mass with hub body . . . . .	16
2.1.5 Internal components . . . . .	17
2.1.6 Other components and additional masses . . . . .	23
2.2 Couplings implementation . . . . .	25
2.2.1 Bearings . . . . .	25
2.2.2 Coupling between shafts . . . . .	26

---

<b>3</b>	<b>Contacts between system components</b>	<b>27</b>
3.1	Motor - Hub . . . . .	28
3.1.1	How it changed . . . . .	29
3.2	Bearing housing - Hub . . . . .	32
3.2.1	How it changed . . . . .	33
3.3	Vanes - Vanes carrier . . . . .	36
3.3.1	How it changed . . . . .	37
<b>4</b>	<b>Results</b>	<b>40</b>
4.1	Reliability of the models . . . . .	40
4.2	Original model . . . . .	41
4.3	Motor's contact . . . . .	42
4.4	Bearing housing's contact . . . . .	44
4.5	Flanged side's contact . . . . .	45
4.6	Vanes contacts . . . . .	46
4.7	Flatness modification . . . . .	48
4.8	Graphs and modes details . . . . .	49
<b>5</b>	<b>Conclusion</b>	<b>54</b>
	<b>References</b>	<b>56</b>
	<b>Appendix A Datasheet</b>	<b>57</b>
A.1	BK6 . . . . .	57
A.2	XTreMA . . . . .	59

# List of Figures

1.1	Mesh example . . . . .	5
1.2	AWT overview [1] . . . . .	9
1.3	AWT with integrated sound generator [1] . . . . .	10
1.4	Details of the system . . . . .	11
1.5	Middle section of the main body . . . . .	11
1.6	Coupling mechanism between the two shafts . . . . .	12
1.7	general view of the test section . . . . .	12
2.1	General view of the first model . . . . .	14
2.2	General view of the second model . . . . .	15
2.3	General view of the third model . . . . .	16
2.4	General view of the fourth model . . . . .	16
2.5	Surfaces inside the hub body . . . . .	17
2.6	Implementation of the vanes, the bearing housing, the rotor and the motor . . . . .	18
2.7	Bearing housing simplification . . . . .	19
2.8	Rotor's shaft simplification . . . . .	20
2.9	Vanes simplification . . . . .	21
2.10	Detail of vanes simplification . . . . .	22
2.11	Final version of the structure . . . . .	23

---

2.12	Surfaces to which additional masses are related . . . . .	24
2.13	Bearings of the system . . . . .	25
2.14	Coupling system between the shafts . . . . .	26
3.1	View of the two contact areas of the motor . . . . .	28
3.2	Deformed configuration of the motor profile . . . . .	29
3.3	One quarter of motor's profile in contact . . . . .	30
3.4	Motor's flange surface in contact . . . . .	30
3.5	Circular-shaped surfaces around the holes of the motor . . . . .	31
3.6	View of the two contact areas of the Bearing housing . . . . .	32
3.7	Deformed configuration of the bearing housing profile . . . . .	33
3.8	One quarter of bearing housing's profile in contact . . . . .	34
3.9	Bearing housing's flange in contact . . . . .	34
3.10	Circular-shaped surfaces around the holes of the bearing housing . . . . .	35
3.11	Vanes and their substructure . . . . .	36
3.12	Inner ring inserted into the hub body . . . . .	37
3.13	Vanes and their carriers . . . . .	38
3.14	Translational joints . . . . .	38
3.15	Cylindrical joints . . . . .	39
4.1	Lateral view of mode 8 . . . . .	46
4.2	Front view of the vanes on mode 9 . . . . .	47
4.3	Lateral view of mode 3 . . . . .	51
4.4	Mode 4 . . . . .	51
4.5	Frequency graphs of modes 8 (a) and 9 (b) . . . . .	52
4.6	Frequency graphs of modes 10 (a) and 11 (b) . . . . .	53
4.7	Mode 10 (a) and mode 11 (b) . . . . .	53

# List of Tables

2.1	Stiffness data of bushing joint between shafts . . . . .	26
4.1	Results of the model with all the components . . . . .	42
4.2	Results of the different contact version of the motor . . . . .	43
4.3	Results of the implementation of different contact version of the bearing housing . . . . .	44
4.4	Results of the implementation of the flanged side's contact . . . . .	45
4.5	Results of the implementation of the vanes contacts . . . . .	47
4.6	Results of the implementation of the flatness modification . . . . .	48
4.7	Results of every model created . . . . .	49
4.8	Variation of each version compared to the original model . . . . .	50
4.9	Percentage difference between models . . . . .	52

# Chapter 1

## Introduction

This thesis presents the study I conducted at the University of Hannover, specifically within the Department of Turbomachinery and Fluid Dynamics. This department houses an acoustic wind tunnel that serves as a test bench for various experiments and its components can be modified and frequently updated depending on current needs. A major modification of the test section, which initiated this project, is planned for 2025. The idea for this study arose from the necessity of re-designing the acoustic wind tunnel, with a particular focus on modifying the section containing the turbine, which has been the subject of previous analyses. In this context, my work was focused on the modal analysis of the future test section. Specifically, I examined the influence of various contact scenarios on defined surfaces of interest between different components. This analysis was used to predict and potentially prevent vibration related issues within the section. The rotation of the turbine blades acts as an excitation source for the rest of the system's components, making it essential to ensure that the resonance frequencies of the entire section do not coincide with the operating frequencies of the turbine. In addition, no construction is entirely free of geometric and dimensional inaccuracies, which inevitably modify the dynamic behaviour of the system. For this reason, each contact between components was carefully analysed and, if necessary, modified to reflect a plausible deformation. This approach allowed for an evaluation of the dynamic behaviour, stiffness, and natural frequencies of the system in the most realistic scenario possible, helping to prevent potential issues during the testing phase once the section is fully assembled.

### 1.0.1 Modal Analysis

The real-life experiment on modal analysis examines the dynamic behaviour of systems in the frequency domain by mechanically exciting a component to highlight its structural modes and recording vibration data with a sensor network. Modern experimental modal analysis systems consist of sensors like accelerometers or load cells, data acquisition systems with analog-to-digital converters for digitizing signals, and a host computer for data visualization and analysis. Traditionally, modal analysis used a SIMO (single-input, multiple-output) approach, where one excitation point generated responses measured at multiple points. Similarly, MISO (multiple-input, single-output) methods, such as hammer surveys, utilized a fixed accelerometer and a hammer. Recent advancements have made MIMO (multi-input, multiple-output) analysis more practical. MIMO uses partial coherence analysis to differentiate responses from various excitation sources, often employing multiple shakers to uniformly distribute energy across a structure for better measurement coherence. Single shakers, by contrast, may fail to excite all structural modes effectively. Excitation signals in modal analysis can include impulse, broadband, swept sine, chirp, and others, each with unique benefits and limitations. Signal analysis typically employs Fourier analysis to derive transfer functions, revealing resonances characterized by mass, frequency, and damping ratios.

Mathematically, the analysis of the system's motion can be conducted directly in the configuration space, typically leads to eigensystems, where the eigenvalues and eigenvectors represent the natural frequencies and their corresponding mode shapes. The analysis starts from the homogeneous equation of motion, given by:

$$M\ddot{x} + Kx = 0. \quad (1.1)$$

This represents a system of linear, second-order homogeneous differential equations. These equations are typically coupled since at least one of the matrices,  $M$  (mass matrix) or  $K$  (stiffness matrix), is not diagonal.

To solve this system, we assume a solution in the Laplace domain, analogous to previous formulations:

$$x = x_0 e^{st}, \quad (1.2)$$

leading to an eigenvalue problem. Since the system is undamped, all solutions  $s$  are purely imaginary. A more convenient approach is to express the solution explicitly in the frequency domain as:

$$x = x_0 e^{i\omega t}. \quad (1.3)$$

By differentiating twice with respect to time, we obtain the acceleration:

$$\ddot{x} = -\omega^2 x_0 e^{i\omega t}. \quad (1.4)$$

Substituting this into the equation of motion results in the algebraic equation:

$$(K - \omega^2 M) x_0 = 0. \quad (1.5)$$

For a non-trivial solution ( $x_0 \neq 0$ ), the determinant of the coefficient matrix must be zero:

$$\det(K - \omega^2 M) = 0. \quad (1.6)$$

This equation defines an eigenvalue problem that can be rewritten in standard form in either of the following ways:

$$\det\left(K^{-1}M - \frac{1}{\omega^2}I\right) = 0, \quad \det(M^{-1}K - \omega^2 I) = 0. \quad (1.7)$$

These characteristic equations are algebraic and of degree  $n$  in  $\omega^2$ , yielding  $n$  distinct natural frequencies. The eigenvalue solutions include both positive and negative frequencies ( $\pm\omega_n$ ), but in most cases, only the positive values are considered. The eigenvectors associated with these eigenvalues define the mode shapes, which describe how different parts of the system oscillate at a given natural frequency.

Since all eigenvalues of  $\omega^2$  are real and positive, the natural frequencies themselves are real.

By collecting all eigenvectors into a square matrix,

$$\Phi = [q_1, q_2, \dots, q_n], \quad (1.8)$$

we can express the complete solution as a superposition of modes:

$$x = \sum_{i=1}^n (K_i^* q_i \cos(\omega_i t) - K_i^* q_i \sin(\omega_i t)). \quad (1.9)$$

The coefficients  $K_i^*$  are determined from the initial conditions, assuming known initial positions  $x_0$  and velocities  $\dot{x}_0$ :

$$\{K_i^*\} = \Phi^{-1} x_0, \quad \{\omega_i K_i^*\} = -\Phi^{-1} \dot{x}_0. \quad (1.10)$$

In an idealized conservative system, free vibrations persist indefinitely without decay. However, real-world systems always exhibit some level of damping, meaning that oscillations eventually decrease over time. [2]

Modal analysis results are often correlated with finite element analysis (FEA). The purpose is to identify the natural mode shapes and frequencies of a structure during free vibration and the finite element method (FEM) is commonly used for this analysis due to its ability to handle objects of arbitrary shapes and produce reliable results.

## 1.1 The Finite Element Method

The finite element method (FEM) is a widely used numerical approach for solving differential equations that arise in engineering and mathematical modelling. It is commonly applied in areas such as structural analysis, heat transfer, fluid dynamics, mass transport, and electromagnetic potential.

FEM is a versatile technique designed to address partial differential equations in two or three spatial dimensions, often associated with boundary value problems.

To solve a problem, FEM breaks down a complex system into smaller, more manageable components called finite elements. This is accomplished through spatial discretization, which involves creating a mesh, a network of finite points that defines the numerical domain for the solution. Dividing a domain into simpler parts offers several benefits, including the ability to accurately model complex geometries, account for different material properties, represent the overall solution effectively, and capture localized effects.

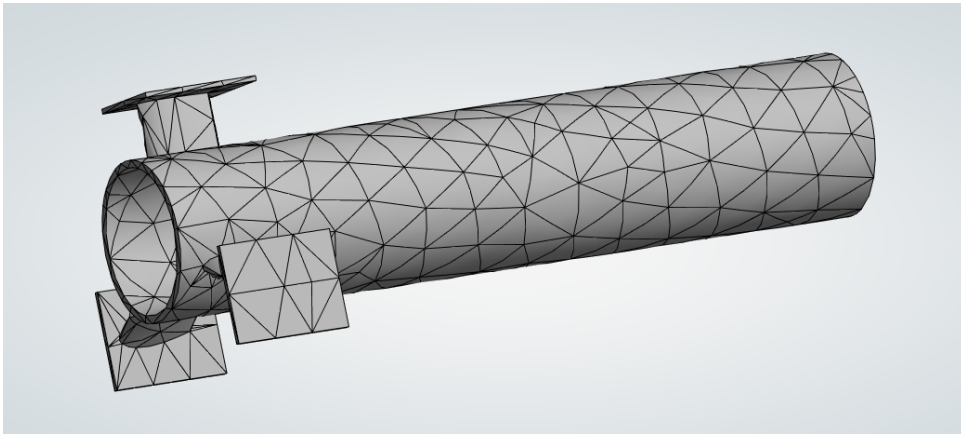


Fig. 1.1 Mesh example

FEM is often formulated using matrix notation, facilitating its implementation in computational algorithms. The displacement field within an element is typically expressed as:

$$u(x, y, z, t) = N(x, y, z)q(t), \quad (1.11)$$

where  $q(t)$  is a vector containing the generalized coordinates of the element, and  $N(x, y, z)$  is a matrix of shape functions. The number of rows in  $N$  corresponds to the number of displacement components, while the number of columns matches the degrees of freedom of the element. In most cases, the degrees of freedom correspond to the displacements at specific locations, referred to as nodes.

Under this assumption:

$$\begin{bmatrix} u_x(x, y, z, t) \\ u_y(x, y, z, t) \\ u_z(x, y, z, t) \end{bmatrix} = \begin{bmatrix} N(x, y, z) & 0 & 0 \\ 0 & N(x, y, z) & 0 \\ 0 & 0 & N(x, y, z) \end{bmatrix} \begin{bmatrix} q_x(t) \\ q_y(t) \\ q_z(t) \end{bmatrix}. \quad (1.12)$$

Here, the displacements in each direction depend only on the corresponding nodal displacements. The matrix  $N$  has a single row and as many columns as the number of nodes in the element. While this formulation is presented for a three-dimensional element, similar expressions apply to one- and two-dimensional elements. Each finite element essentially models a small deformable solid. Its behaviour is analysed using an assumed-modes approach, where a limited number of degrees of freedom replace the infinite degrees of freedom present in a continuous domain. The displacement field within an element is approximated as a linear combination of arbitrarily chosen shape functions. They are chosen with a degree of freedom, but they must satisfy several conditions:

- They must be continuous and differentiable to the required order, depending on the element type.
- They must be able to describe rigid-body motions, ensuring zero elastic potential energy.
- They should enable a constant strain field when required by the overall deformation.
- They must ensure that adjacent elements deform compatibly at their interfaces.

The last condition ensures that when the nodes of neighboring elements move consistently, the entire structure deforms cohesively. Additionally, an ideal shape function should be isotropic, meaning its properties should not depend on the choice of the reference frame.

The motion of an element can be derived following the assumed-modes methodology. The strain field can be expressed in terms of displacement derivatives:

$$\boldsymbol{\varepsilon}(x, y, z, t) = \boldsymbol{B}(x, y, z) \boldsymbol{q}(t), \quad (1.13)$$

where  $\varepsilon$  is a column matrix containing the strain tensor components, and  $B(x, y, z)$  is a matrix containing the derivatives of the shape functions. The number of rows in  $B$  corresponds to the number of strain components, while the number of columns matches the element's degrees of freedom.

Assuming the element is free from initial stresses and follows linear material behaviour, the stress field is given by:

$$\sigma(x, y, z, t) = E\varepsilon = E(x, y, z)B(x, y, z)q(t), \quad (1.14)$$

where  $E$  is the material stiffness matrix, typically a symmetric square matrix that may depend on spatial coordinates but is often assumed constant within an element. The element's potential energy is given by:

$$U = \frac{1}{2} \int_V \varepsilon^T \sigma dV = \frac{1}{2} q^T \left( \int_V B^T E B dV \right) q. \quad (1.15)$$

This integral defines the element stiffness matrix:

$$K = \int_V B^T E B dV. \quad (1.16)$$

Since shape functions do not vary with time, generalized velocities take the form:

$$\dot{u}(x, y, z, t) = N(x, y, z)\dot{q}(t). \quad (1.17)$$

When generalized coordinates represent displacements, the kinetic energy and mass matrix are expressed as:

$$T = \frac{1}{2} \int_V \rho \dot{u}^T \dot{u} dV = \frac{1}{2} \dot{q}^T \left( \int_V \rho N^T N dV \right) \dot{q}, \quad (1.18)$$

where the mass matrix is:

$$M = \int_V \rho N^T N dV. \quad (1.19)$$

In cases where generalized coordinates involve rotations, modifications are required to incorporate moments of inertia, although the general formulation remains unchanged.

If a force distribution  $f(x, y, z, t)$  is applied to the structure, the virtual work associated with a virtual displacement  $\delta u = N\delta q$  leads to:

$$\delta L = \int_V \delta u^T f dV = \int_V \delta q^T N^T f dV. \quad (1.20)$$

From this, the nodal force vector is given by:

$$f(t) = \int_V N^T f dV. \quad (1.21)$$

The element's equation of motion follows the standard form for discrete undamped systems:

$$M\ddot{q} + Kq = f(t). \quad (1.22)$$

This equation illustrates how the finite element method (FEM) provides a discretized formulation of the general equation of motion used in modal analysis (eq. 1.0.1). Through detailed numerical modelling of the structure, FEM enables the computation of the mass matrix  $M$  and the stiffness matrix  $K$ . When no external forces are applied, the equation aligns precisely with that of modal analysis (eq. 1.0.1). In conclusion, FEM and modal analysis serve as complementary tools for studying the vibrational and dynamic behaviour of structures, particularly in cases involving complex geometries and heterogeneous materials. [2]

## 1.2 Aeroacoustic Wind Tunnel

As mentioned above, the study focuses on the Aeroacoustic Wind Tunnel of the Department of Turbomachinery and Fluid Dynamics. This is a specialized testing facility designed for studying aeroacoustic phenomena in ducts and turbomachines.

The test section can be substituted with various modules, including sound absorbers, instrumented test sections, or even rotating turbine or compressor stages, allowing these components to be examined under controlled inflow conditions.



Fig. 1.2 AWT overview [1]

The main fields of application are:

- Investigation of aeroacoustic generation and transport mechanisms in circular ducts;
- Testing of acoustic duct liners;
- Testing and optimization of acoustic and aerodynamic instrumentation and sensors;
- Testing and validation of measurement techniques and analysis routines;
- Validation of numerical models

The present project focuses on examining acoustic transport mechanisms in tubes and turbomachinery. To support this investigation, an acoustic excitation system was integrated into the AWT test section to generate synthetic acoustic fields. These fields propagate through the test section, creating varying acoustic pressure fields that are measured at different locations. The resulting measurements provide insights into the transport mechanisms. [1]

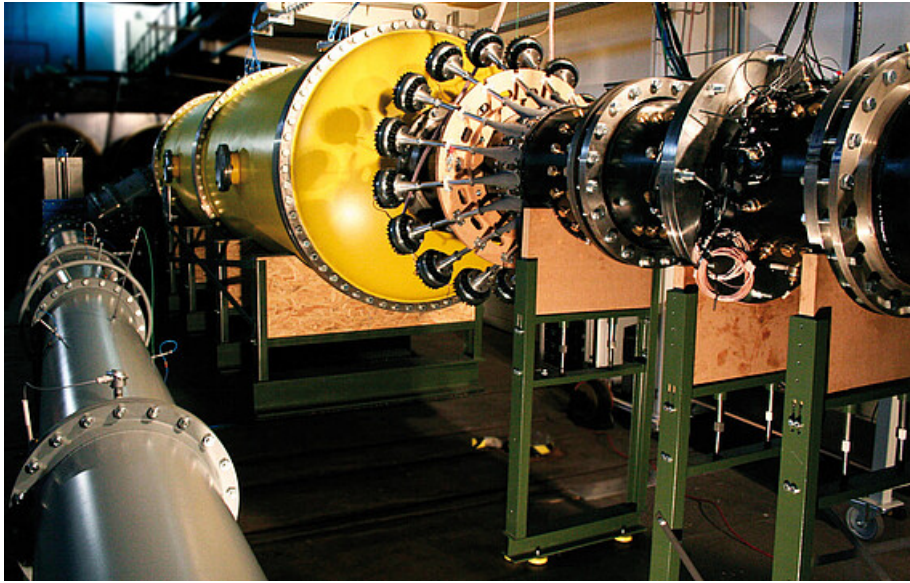


Fig. 1.3 AWT with integrated sound generator [1]

### 1.2.1 Test section

The current configuration of the test section, consist of a turbomachine. In detail, it includes:

- the impeller and guide wheel of a typical low-pressure turbine
- the motor
- the bearings housing
- a coupling mechanism with a torque meter
- the hub body
- the external case

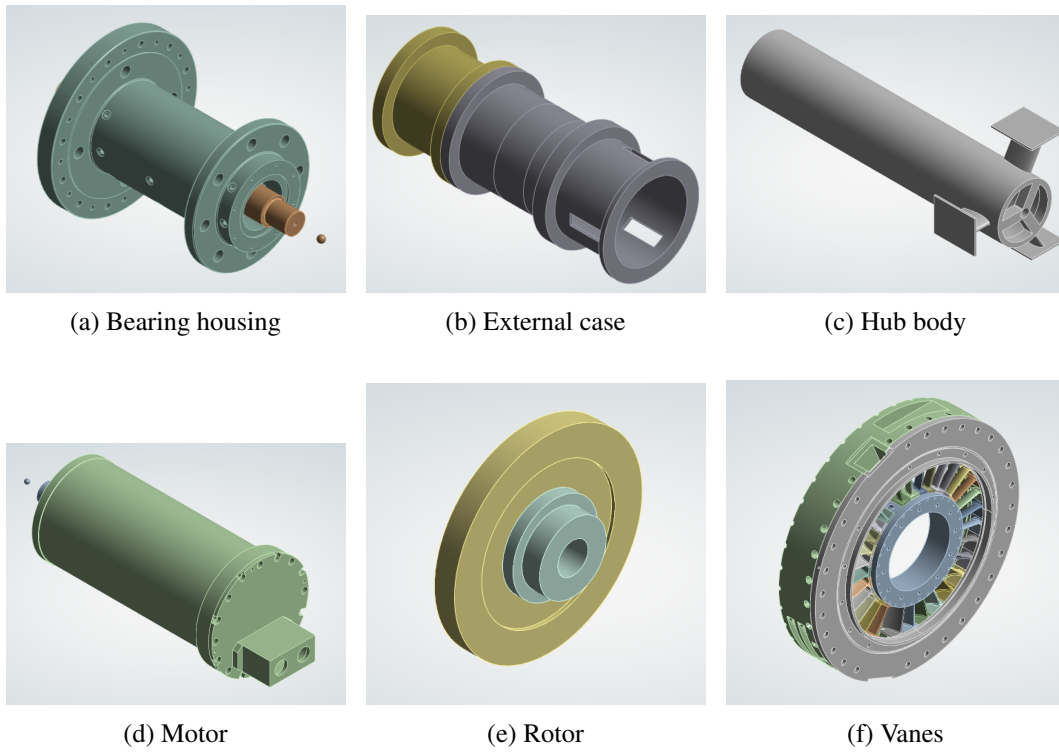


Fig. 1.4 Details of the system

The following figure represents the middle section of the described parts:

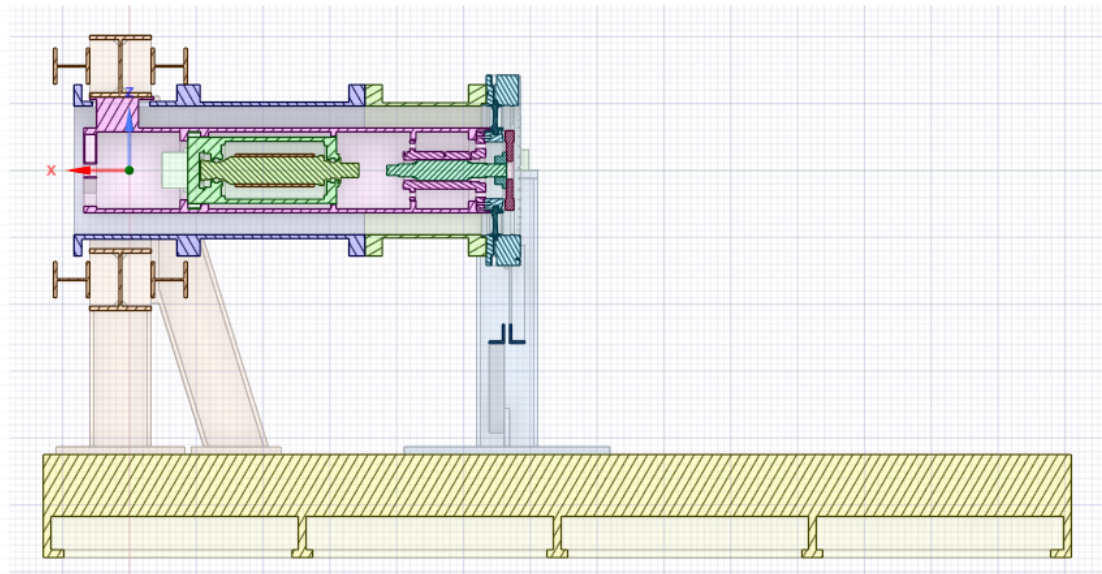


Fig. 1.5 Middle section of the main body

The shafts connect the motor (on the left-hand side of the figure) to the rotor, represented by the inner vanes carrier, through the hub body. The coupling mechanism between the two shafts is not shown in the figure, as it will be modelled as a specific joint in later steps. However, it consists of:

- Bellows coupling with external clamping ring and tapered press-fit connection
- Torque measuring flange



(a) Coupling mechanism BK6 [3]



(b) Torque meter Xtrema [4]

Fig. 1.6 Coupling mechanism between the two shafts

The complete test section also includes the structure to be fixed to the ground.

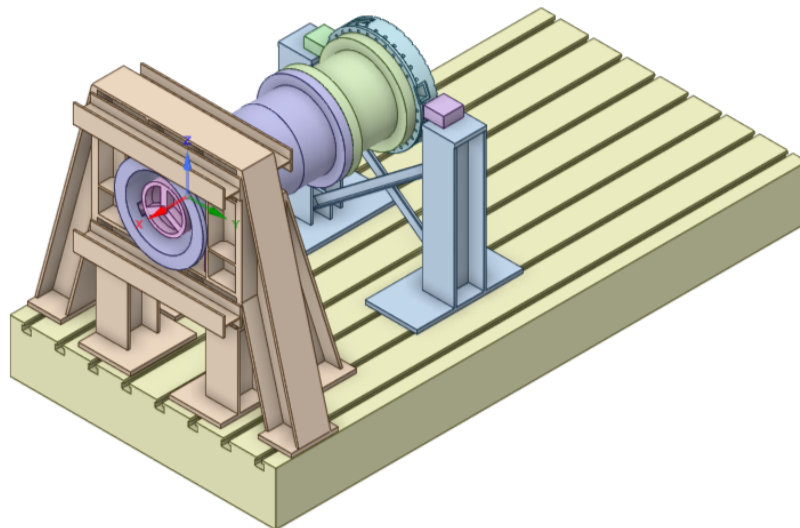


Fig. 1.7 general view of the test section

# Chapter 2

## Models

### 2.1 Basic models

Starting from the original CAD file, several models were developed with progressively increasing complexity, ranging from the simplified structure to the complete model, including all components and couplings. Understanding the influence of these changes and their effect on the frequencies and vibration modes of the entire system was very important. Components were added in the following order:

- Main structure
- Hub body
- Vanes
- Bearing housing
- Motor
- Additional masses
- Bearings
- Coupling system

### 2.1.1 Central mass

The first model is represented here:

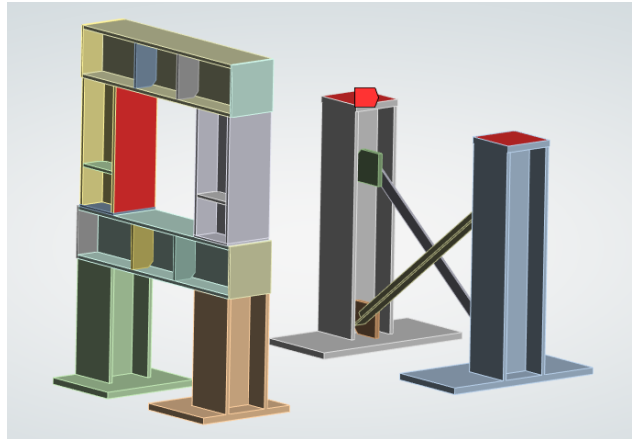


Fig. 2.1 General view of the first model

It consists of the simplified structure without the hub and the components inside it. These components were replaced with a mass uniformly distributed over the red surfaces shown in the figure. In addition, the foundation was removed and replaced with fixed supports located below the two substructures. All components are made of steel, except for the vanes and rotor, which are made of aluminium. After evaluating the volumes of the components, the total added mass amounts to 585 *kg*, distributed as follows:

- 163 *kg* for the motor and its shaft
- 232 *kg* for the hub body
- 90 *kg* for the vanes
- 44 *kg* for the bearing housing
- 20 *kg* for the rotor and its shaft

### 2.1.2 Split mass

The second model is represented here:

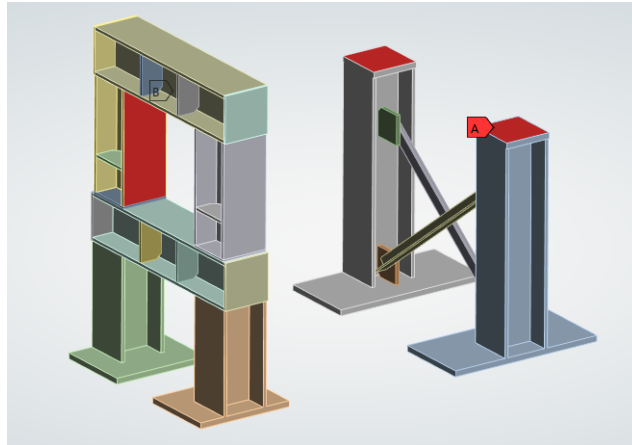


Fig. 2.2 General view of the second model

Compared to the first model, the upgrade involves dividing the mass to account for its unequal distribution. Half of the hub, the motor, and its shaft were assigned to the surfaces labeled "B." The other half of the hub, along with the bearing housing, the rotor, its shaft, the vanes, and their carrier, were assigned to the surfaces labeled "A", this results in 279 kg for the left hand side of the structure and 306 kg for the right hand side.

### 2.1.3 Split mass with bonded contact

In the third model, the components are still represented as distributed mass. However, the two substructures are now bonded together using a Boolean operator available in ANSYS, which creates a unified structure. This modification marks a significant step in the modelling process, as it introduces a more realistic interaction between the substructures, the masses are still divided as described before. It is represented in the figure 2.3.

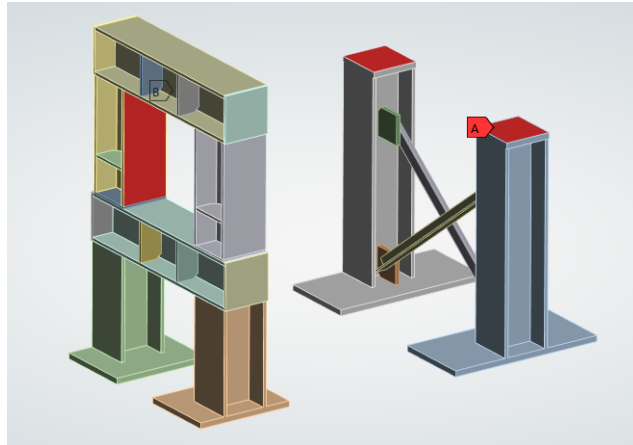


Fig. 2.3 General view of the third model

#### 2.1.4 Split mass with hub body

The fourth model is represented here:

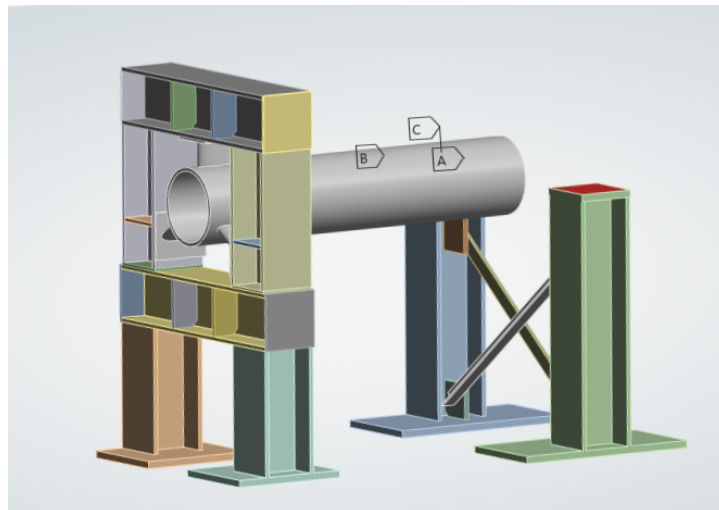


Fig. 2.4 General view of the fourth model

The hub was added to the model, and its mass was removed from the distributed ones. It was then fixed on the left-hand side of the figure using three bonded contacts and connected to the shorter of the two substructures with a Boolean operator. The masses of the components are no longer associated with the previous surfaces, as they can now be placed in their precise locations inside the hub body.

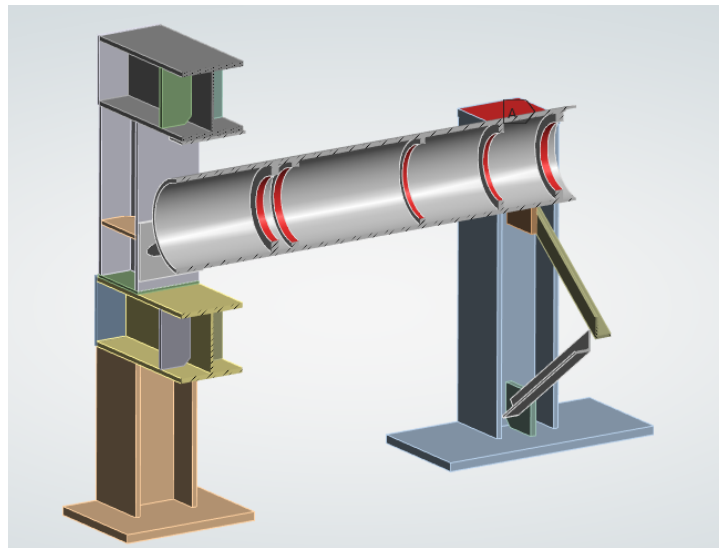
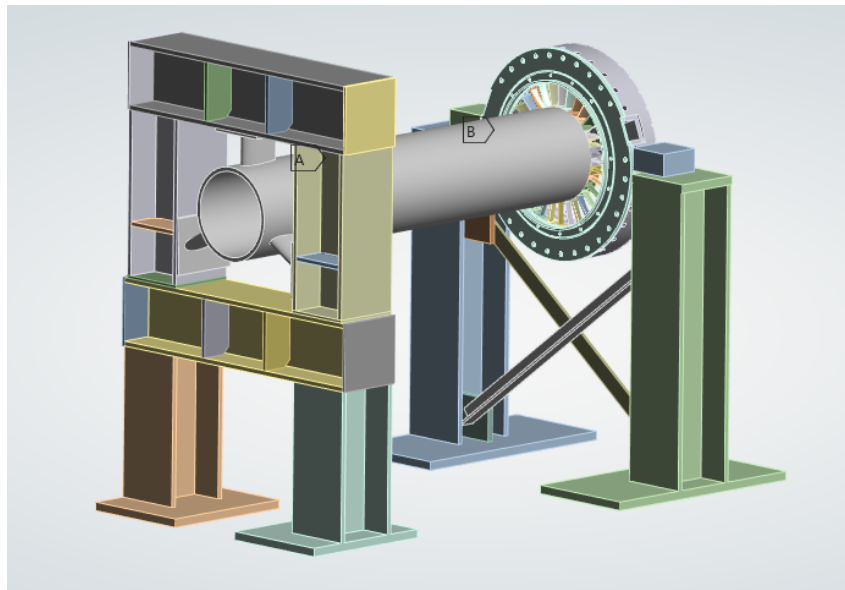


Fig. 2.5 Surfaces inside the hub body

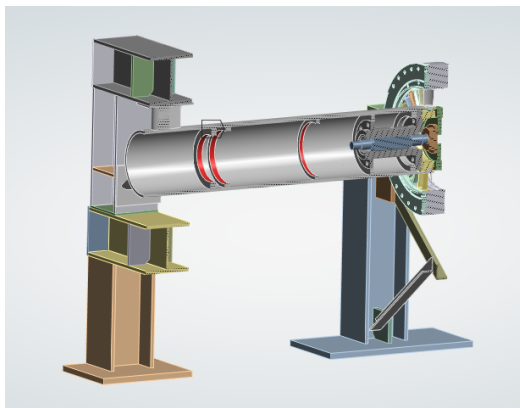
The mass of the motor and its shaft was assigned to the first three ribs on the left-hand side, while the mass of the bearing housing and the rotor shaft was associated with the last two ribs. Additionally, the mass of the vanes and their carrier was distributed over the red-highlighted surfaces in the smaller substructure.

### 2.1.5 Internal components

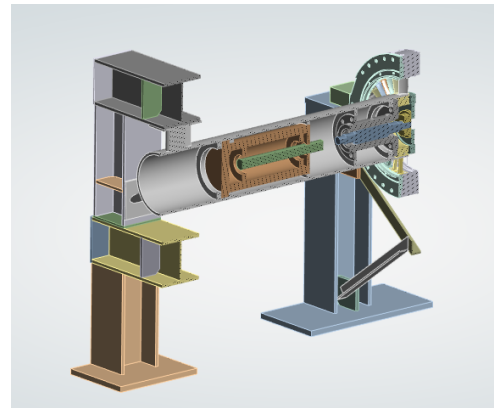
The vanes, their carrier, the rotor, the motor, the bearing housing, and their shaft were added to the model, replacing the previously used distributed masses. This change allows for a more detailed representation of each component, with their individual properties now being taken into account. The models are represented in the figure 2.10.



(a) Vanes



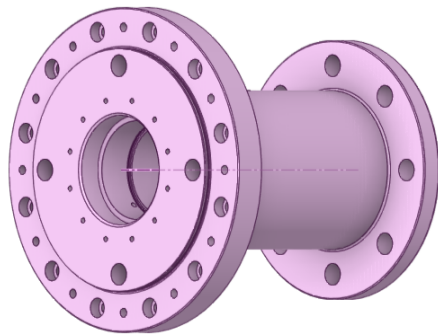
(b) Bearing housing and rotor



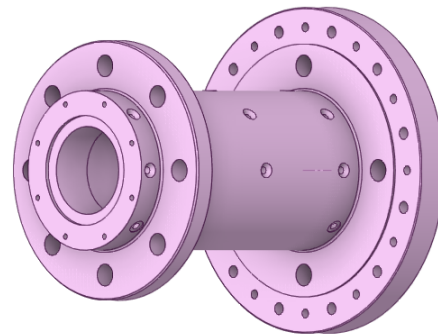
(c) Motor

Fig. 2.6 Implementation of the vanes, the bearing housing, the rotor and the motor

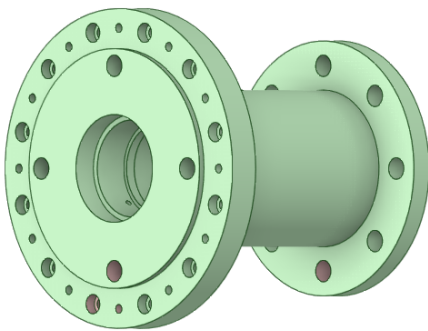
The components were simplified before being incorporated by removing the smallest details. Specifically, all features that would have necessitated an extremely fine mesh, thereby significantly increasing computation time without providing any meaningful benefit in terms of results, were omitted. For instance, very small holes, fillets, or chamfered edges create tiny surfaces that would require exceptionally small mesh elements. As an example, the bearing housing, rotor shaft and vanes are depicted in the following figures.



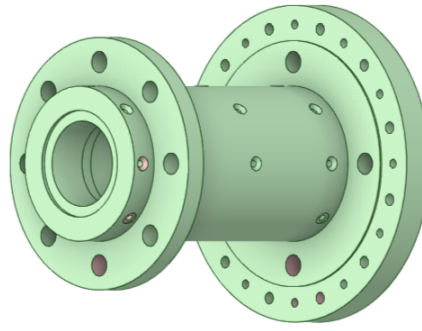
(a) Front view of the original geometry



(b) Rear view of the original geometry



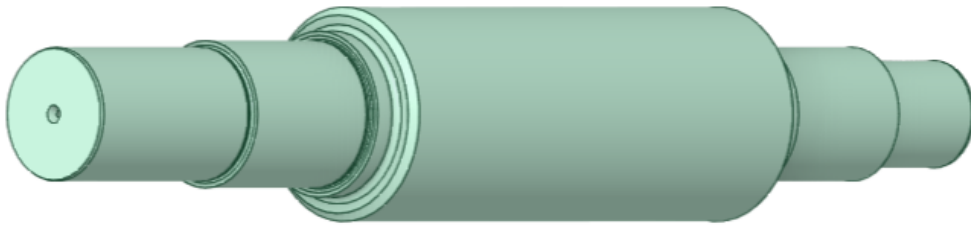
(c) Front view of the simplified geometry



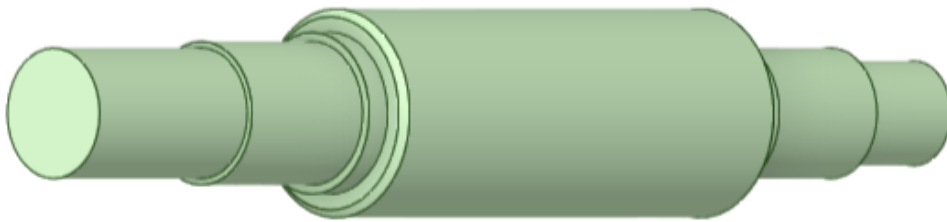
(d) Rear view of the simplified geometry

Fig. 2.7 Bearing housing simplification

The shaft inside the bearing housing has been simplified while preserving its original characteristics and dimensions.



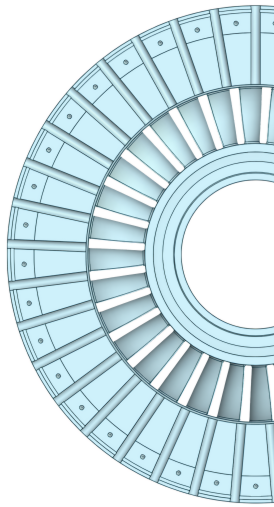
(a) Original



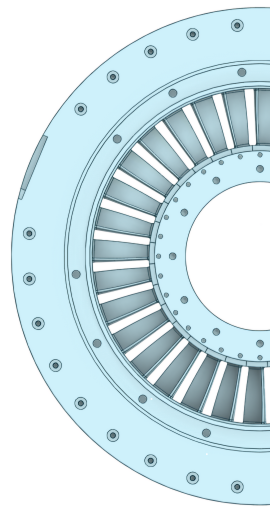
(b) Simplified

Fig. 2.8 Rotor's shaft simplification

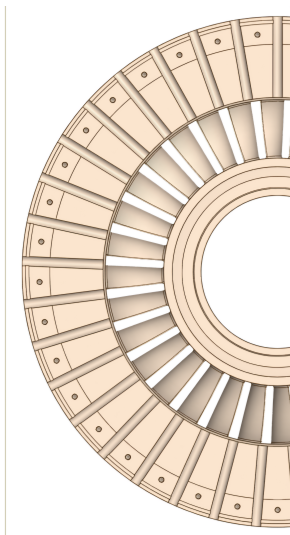
Subsequently, the work continued with the vanes carrier, where both its external and internal details were simplified to optimize the model. At the same time, each individual vane was carefully modified to reduce its complexity while ensuring that its structural rigidity and overall mechanical behaviour remained unchanged.



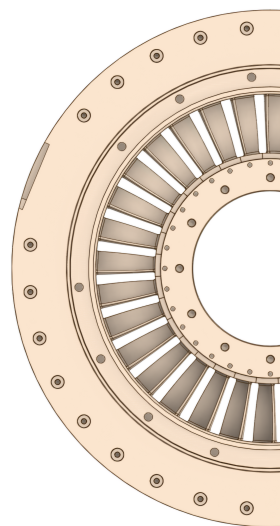
(a) Front view of the original geometry



(b) Rear view of the original geometry



(c) Front view of the simplified geometry



(d) Rear view of the simplified geometry

Fig. 2.9 Vanes simplification

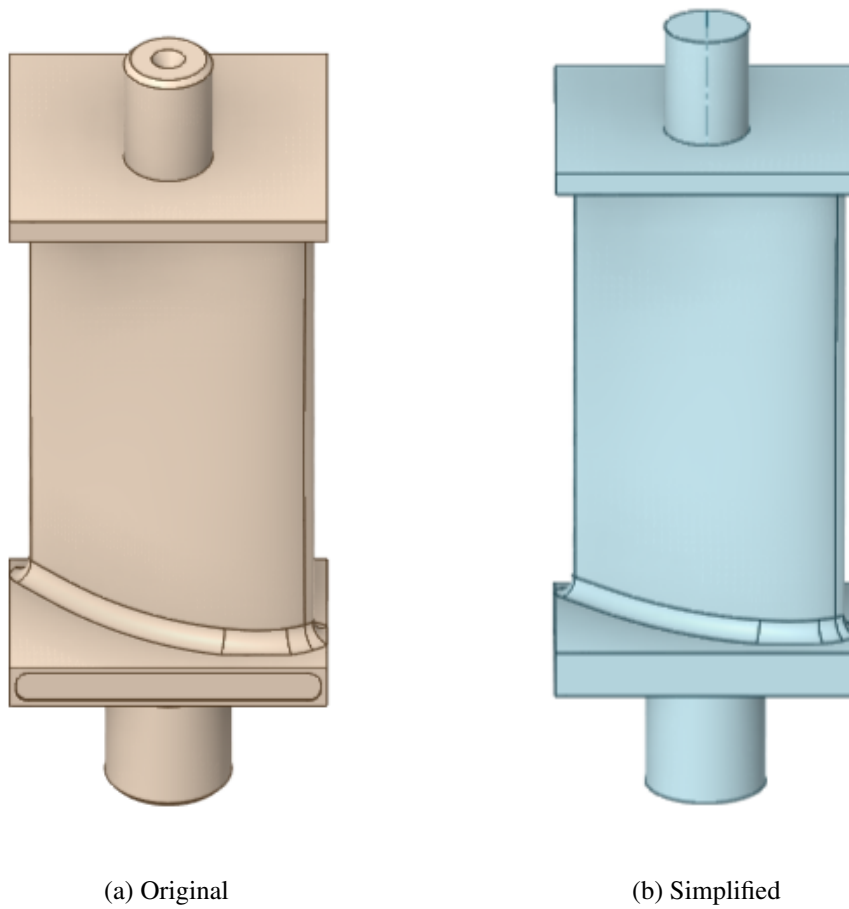


Fig. 2.10 Detail of vanes simplification

The mass of the components is an important factor in modal analysis. The process of removing minor details, which were often filled in during simplification, did not lead to a significant increase in the overall mass of the components. As a result, it was not necessary to restore the mass to its original value, since the changes made were negligible in terms of their effect on the dynamic behaviour of the system.

### 2.1.6 Other components and additional masses

The last details added are the external covers of the test section (Fig. 1.4b), some reinforcements of the structure and a number of additional masses.

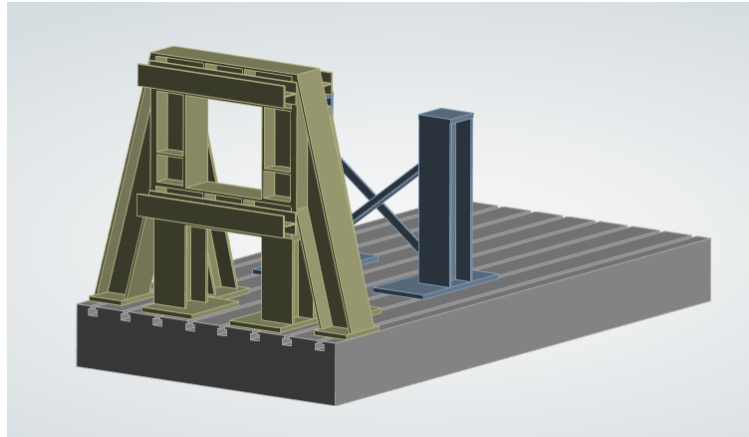
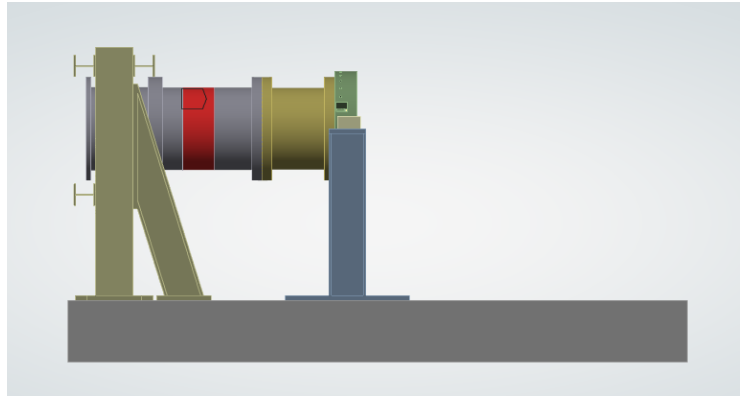


Fig. 2.11 Final version of the structure

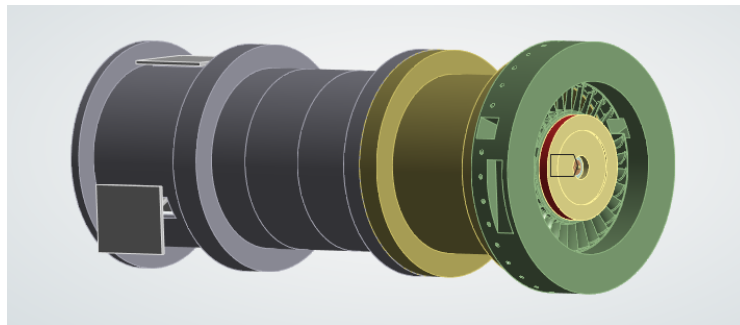
Several additional masses with their moment of inertia were added to the model. In detail:

- The speaker that generate the synthetic acoustic fields:
  - mass: 180 kg
- The blades of the rotor:
  - mass: 3 kg
  - moment of inertia around  $x$  axis: 73926 kg · mm<sup>2</sup>
  - moment of inertia around  $y$  axis: 37644 kg · mm<sup>2</sup>
  - moment of inertia around  $z$  axis: 37644 kg · mm<sup>2</sup>
- The coil of the motor:
  - mass: 8.4 kg
  - moment of inertia around  $x$  axis: 28777 kg · mm<sup>2</sup>
  - moment of inertia around  $y$  axis: 80514 kg · mm<sup>2</sup>
  - moment of inertia around  $z$  axis: 80514 kg · mm<sup>2</sup>

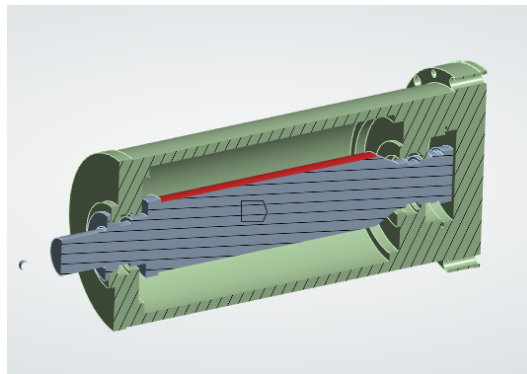
The surfaces to which they refer are as follows:



(a) Speaker



(b) Blades



(c) Coil

Fig. 2.12 Surfaces to which additional masses are related

## 2.2 Couplings implementation

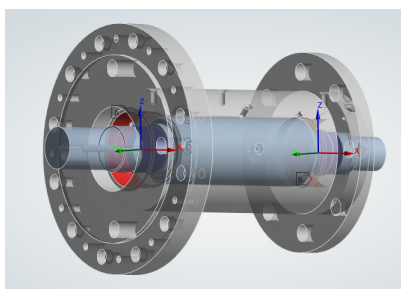
After adding the main components of the system, the bearing mechanism and the coupling between the shafts were implemented.

### 2.2.1 Bearings

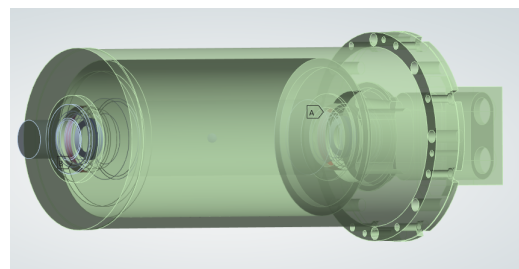
There are four bearings in the system, two of them between the shaft and the motor while the others are located on the bearing housing. They were implemented in ANSYS by means of the connection called "Bearing" and the joint called "Bushing" with the following stiffness data:

- Rotor:
  - $3,12 \cdot 10^8 \text{ N/m}$  radial stiffness
  - $6,36 \cdot 10^8 \text{ N/m}$  radial stiffness,  $1,06 \cdot 10^8 \text{ N/m}$  axial stiffness
- Motor:
  - $2,1 \cdot 10^8 \text{ N/m}$  radial stiffness
  - $2,1 \cdot 10^8 \text{ N/m}$  radial stiffness,  $9,9 \cdot 10^7 \text{ N/m}$  axial stiffness

Their location are represented here:



(a) Rotor's bearings



(b) Motor's bearings

Fig. 2.13 Bearings of the system

## 2.2.2 Coupling between shafts

The coupling between the shafts, as mentioned in Chapter 1, Section 1.2.1, it is a combination of two elements, with different characteristics, details of which can be found in Appendix A. Anyway, it was made in ANSYS using the connection "Joint", then "Bushing", with the following stiffness data:

Stiffness	Per Unit $X$ (mm)	Per Unit $Y$ (mm)	Per Unit $Z$ (mm)
$\Delta$ Force $X$ (N)	$3,4 e5$	-	-
$\Delta$ Force $Y$ (N)	-	$3,4 e5$	-
$\Delta$ Force $Z$ (N)	-	-	105

Table 2.1 Stiffness data of bushing joint between shafts

It is represented here with the coordinate system:

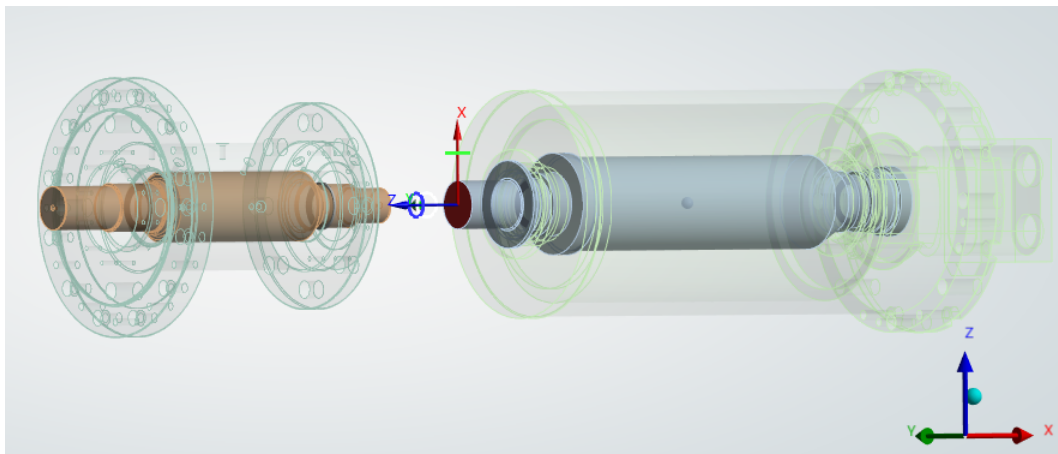


Fig. 2.14 Coupling system between the shafts

Moreover, was added his mass of  $5\text{ kg}$  with a moment of inertia around  $x$  axis of  $5200\text{ kg} \cdot \text{mm}^2$ .

# Chapter 3

## Contacts between system components

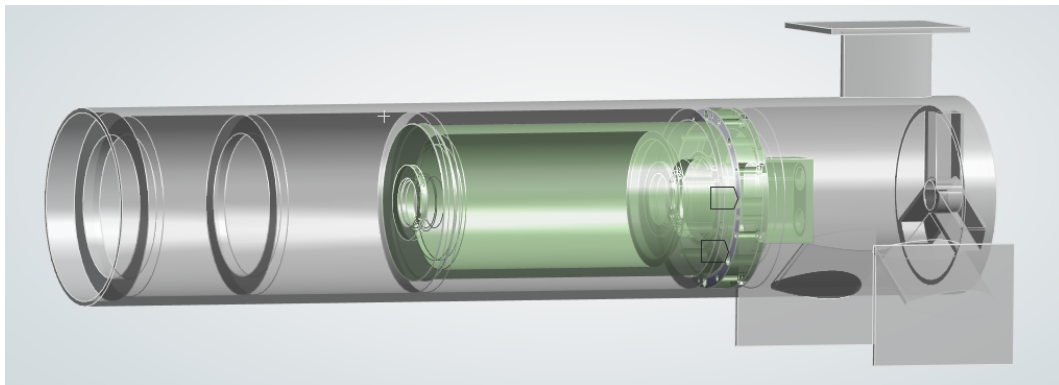
### Overview

The system involves various types of contact. For each component, a specific type was chosen based on its function. The supporting structure, fixed to the ground, consists only of rigid connections, as its parts are either welded or bolted together. This structure is highly rigid and is not a focus of interest for the detailed analysis of the system's dynamics, which is more concerned with the contacts described below. For this reason, no variations in its connections or geometry have been studied, while the most significant contact situations were those involving:

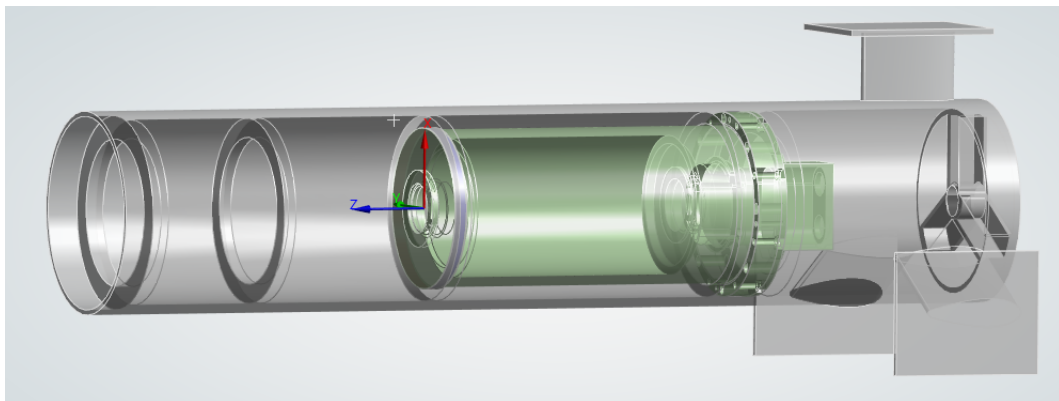
- Motor - Hub
- Bearing housing - Hub
- Vanes - Vanes carrier

### 3.1 Motor - Hub

The motor is situated inside the hub, as shown in Fig. 1.5, or in details in Fig. 1.4d. On one side, it features a flange bolted to the corresponding rib of the hub, while on the other side, it is simply positioned within the space created by another hub rib. This is illustrated here:



(a) Bolted flange



(b) Other side

Fig. 3.1 View of the two contact areas of the motor

These two types of contact were implemented in two different ways: the bolted flange was treated as a bonded contact, while the other side was represented as a cylindrical joint. Variations in geometry and contact areas were introduced to analyse the most realistic scenario possible.

### 3.1.1 How it changed

The primary modification to the motor concerns the non-fixed side, specifically the cylindrical joint. The main goal was to analyse how changes in the contact surface affect the system's stiffness and, consequently, its frequency response. A specific distortion of the motor, and therefore the corresponding hub rib, was assumed. Based on the shaft and hole tolerance system, a plausible deformation was selected. The profiles of the motor and the hub rib were then modified, giving them a pear-shaped design.

For example, about the motor, it has a diameter of  $260\text{ mm}$  and a deformation of  $32\text{ }\mu\text{m}$  was assumed, as shown in the figure:

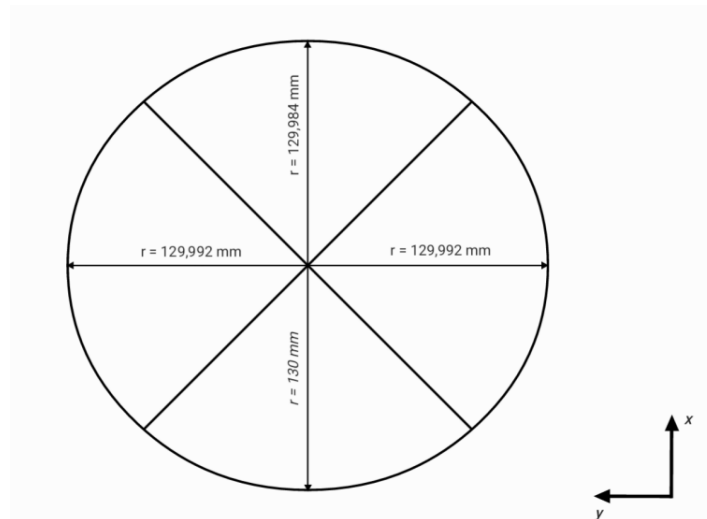


Fig. 3.2 Deformed configuration of the motor profile

As illustrated in the figure, to achieve the pear-shaped design, the profile was divided into four sections, each with a different diameter, the reasons for this approach are as follows:

- this division allows the definition of two main diameters: one slightly distorted and one significantly distorted.
- dividing the surface into additional sections would have been redundant, significantly increasing the number of calculations without offering any benefits.

The analysis was performed using only one-quarter of the profiles of the two components in contact. Initially, only the motor was deformed, and later the hub rib as well. All possible combinations of contact between the surfaces were examined. For example, the region with the largest diameter of the motor was paired with the region of the hub rib that had the smallest diameter, then with the medium diameter, and finally with the non-deformed section. This process was repeated for every possible contact scenario.

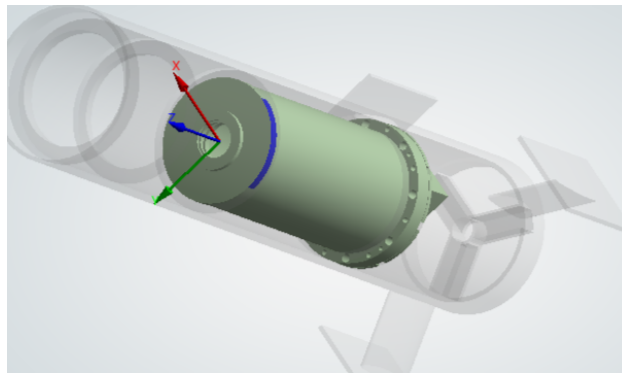


Fig. 3.3 One quarter of motor's profile in contact

In the final configuration chosen, the quarter profile of the motor with the smallest radius was paired with the quarter profile of the hub rib with the largest diameter. Thus, the two areas with the greatest absolute distortion defined the worst contact situation.

On the flanged side, which is bolted to the other hub rib, a bonded contact was selected. Initially, all the surfaces were in contact, as illustrated here:

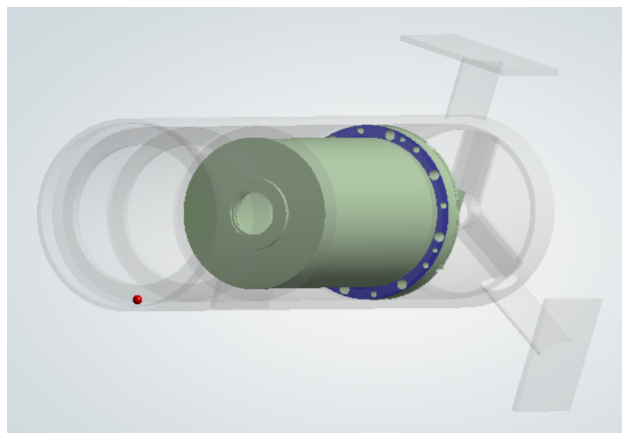


Fig. 3.4 Motor's flange surface in contact

Then, to achieve a more realistic stiffness, different circular-shaped surfaces were created around all the holes needed for the bolts, both in the hub rib and in the motor.

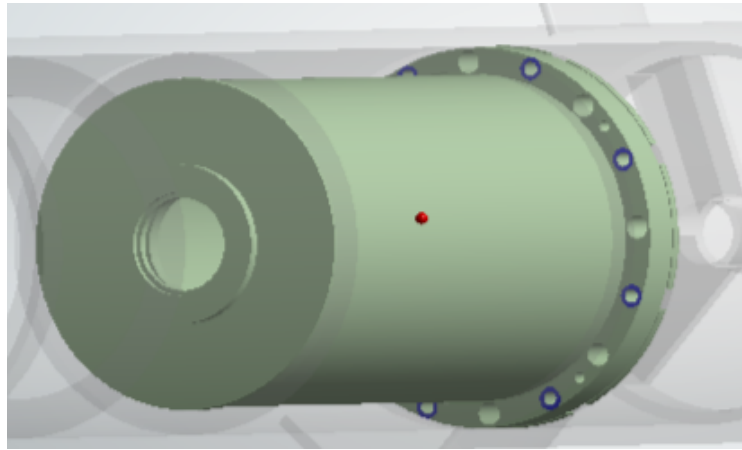
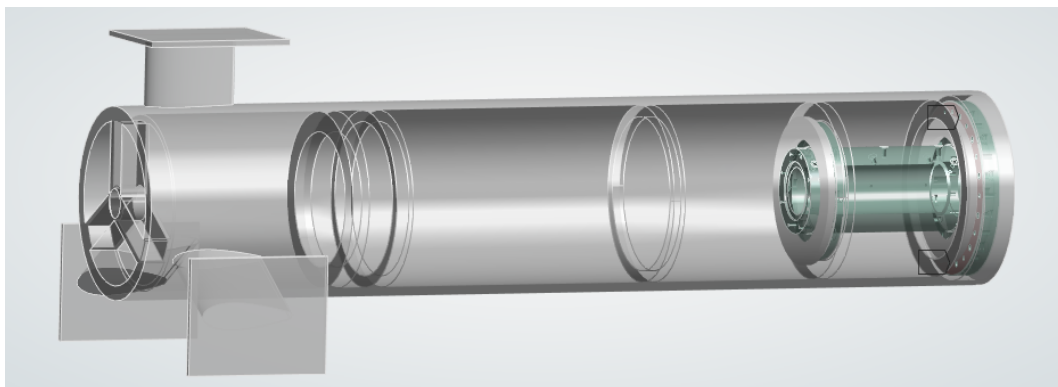


Fig. 3.5 Circular-shaped surfaces around the holes of the motor

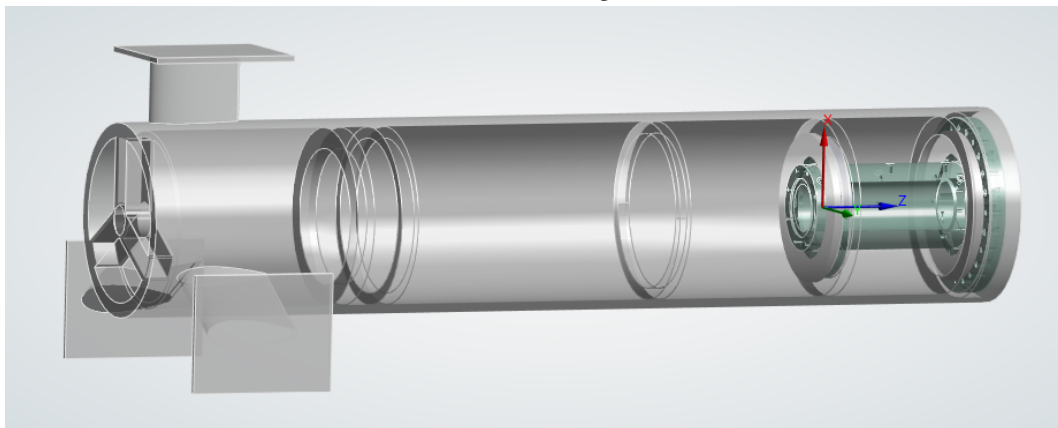
In addition, a final modification was made to simulate a flatness error based on a possible geometric tolerance value. A quarter of the flange surface was placed in a different plane from the original one.

## 3.2 Bearing housing - Hub

The motor is situated inside the hub, as shown in Fig. 1.5, or in details in Fig. 4.7a. On one side it has a flange that is bolted to the correspondent rib of the hub, while on the other side it is only placed within the space created by another hub rib. It is represented here:



(a) Bolted flange



(b) Other side

Fig. 3.6 View of the two contact areas of the Bearing housing

As written before in the section 3.1, these two type of contact were implemented in two different ways:

- Bonded contact for the bolted flange
- Cylindrical joint for the other side

### 3.2.1 How it changed

As with the motor, the primary modification to the bearing housing concerns the non-fixed side, where the cylindrical joint is located. The profiles of the hub rib and the bearing housing were adjusted based on the shaft and hole tolerance system, giving them a pear-shaped design.

About the bearing housing, it has a diameter of  $236\text{ mm}$  and a deformation of  $29\text{ }\mu\text{m}$  was assumed, as shown in the figure:

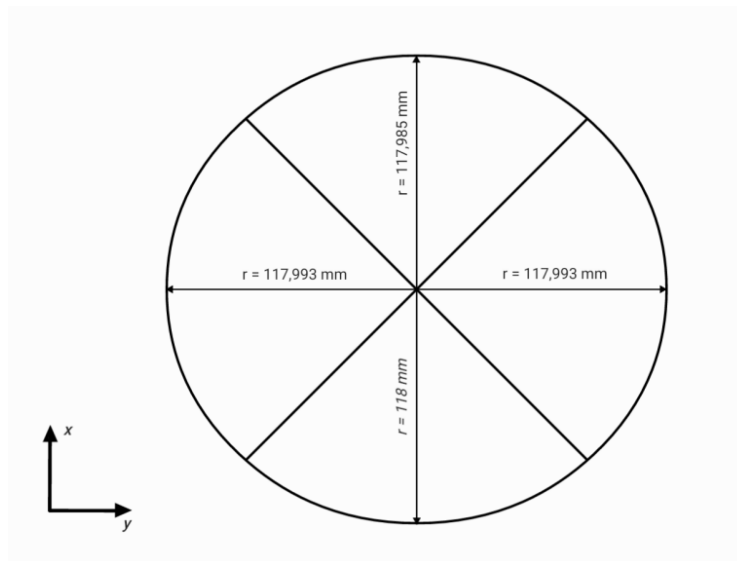


Fig. 3.7 Deformed configuration of the bearing housing profile

The profiles were divided into four sections, each with a different diameter, as explained in the section 3.1.1. The analysis was conducted using only one-quarter of the profiles of the two components in contact. Initially, only the bearing housing was deformed, and later the hub rib as well. Once again, every possible combination of contact between the surfaces was examined and the final configuration chosen consist of: the quarter profile of the bearing housing with the smallest radius paired with the quarter profile of the hub rib with the largest diameter, so the two areas with the greatest absolute distortion. The results of each combination will be presented in the chapter 4.

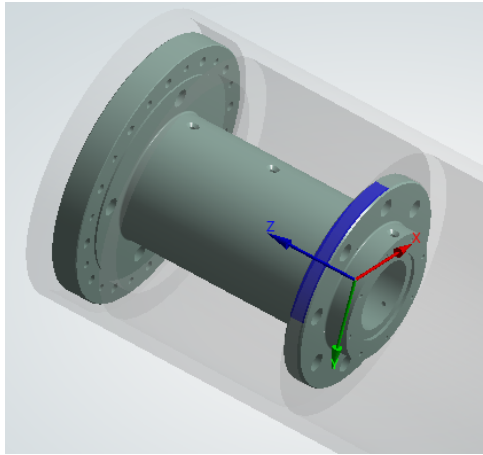


Fig. 3.8 One quarter of bearing housing's profile in contact

With respect to the flanged side, which is bolted to the other hub rib, a bonded contact was chosen. As made for the motor's side, first, all surfaces were in contact as shown here:

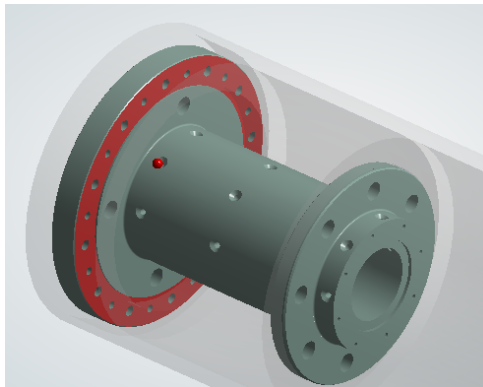


Fig. 3.9 Bearing housing's flange in contact

Then, to achieve a more realistic stiffness, different circular-shaped surfaces were created around all the holes needed for the bolts, both in the hub rib and in the motor.

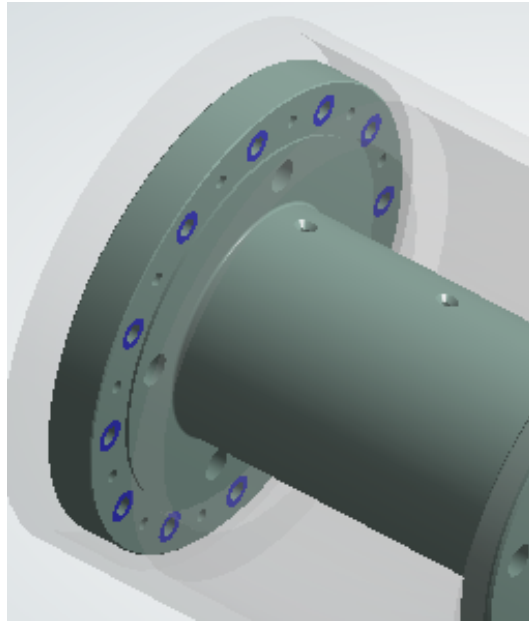


Fig. 3.10 Circular-shaped surfaces around the holes of the bearing housing

Additionally, similar to the approach used for the motor, a final adjustment was made to simulate a flatness error based on a potential geometric tolerance value. Specifically, one-quarter of the flange surface was shifted to a plane different from the original one.

### 3.3 Vanes - Vanes carrier

The vanes and their carriers are positioned at one end of the hub body. The inner ring is inserted into the hub, while the outer ring is fixed to its own substructure, as shown here:

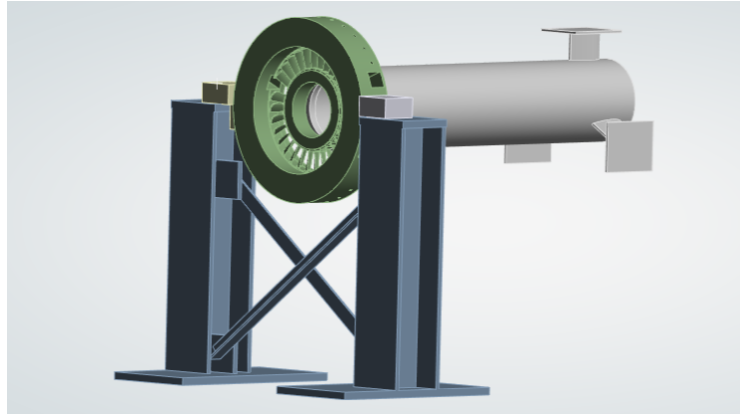


Fig. 3.11 Vanes and their substructure

Two specific vanes were deliberately excluded from the model, as those areas are intended to accommodate sensors. These sensors have significantly lower stiffness compared to the vanes, and their replacement with the vanes themselves could result in an inaccurate estimation of the structure's overall stiffness. Including them in the simulation might have led to an overestimation of the component's stiffness, affecting the reliability of the results. For this reason, the decision was made to conduct the simulations without these two vanes.

Initially, the vanes and their carriers were considered as a single body. Inner ring, vanes and outer ring were fixed to each other.

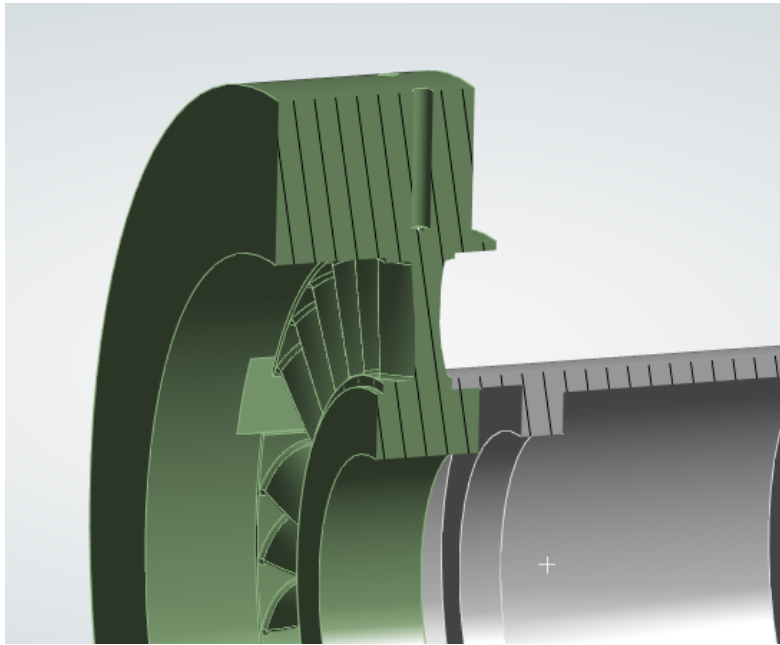


Fig. 3.12 Inner ring inserted into the hub body

### 3.3.1 How it changed

The main changes were focused on the correct connections between the vanes and their carriers at the following contact points defined between vanes and:

- Hub body
- Inner ring
- First out of two outer ring
- Second out of two outer ring that has:
  - one cylindrical housing
  - one vertical rib

First, the vanes and their carriers are represented as different bodies:

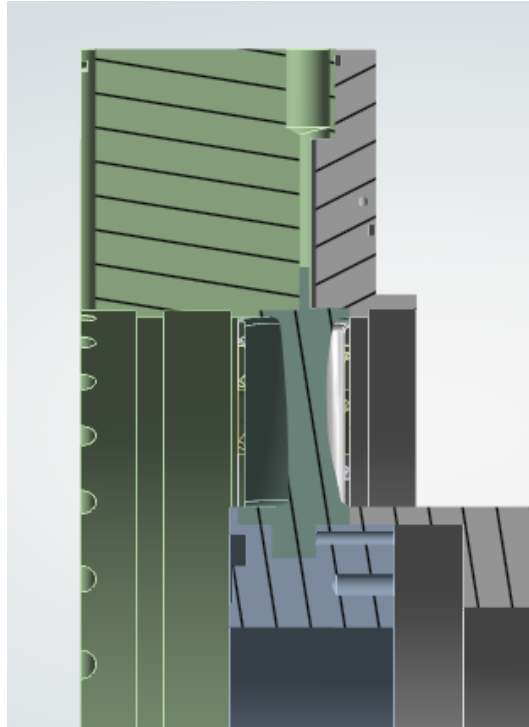
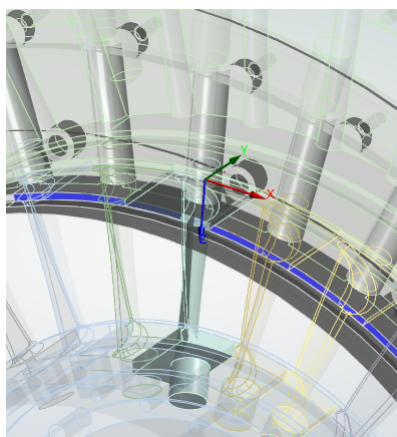
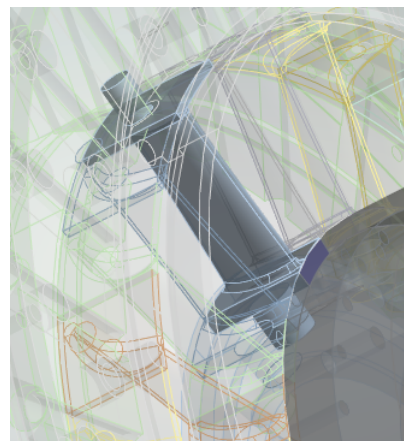


Fig. 3.13 Vanes and their carriers

Two types of joints were selected: translational and cylindrical. The translational joint was used for all the planar surfaces, while the cylindrical joint was applied to the cylindrical surfaces. Specifically, the translational contacts are as follows:



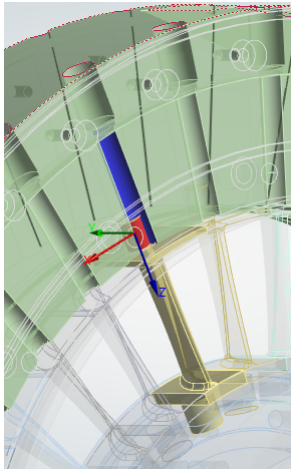
(a) Vanes - Outer ring



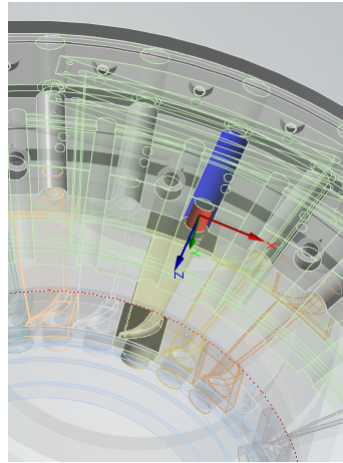
(b) Vane - Hub body

Fig. 3.14 Translational joints

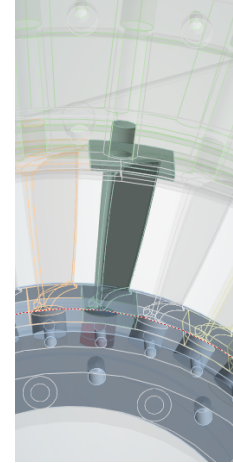
And the cylindrical contacts:



(a) Vane - First Outer ring



(b) Vane - Second Outer ring



(c) Vane - Inner ring

Fig. 3.15 Cylindrical joints

These connections were selected based on the actual behaviour of the vanes. Specifically, they can freely slide and rotate at their cylindrical connection surfaces, while they can translate or slide relative to their supports at their planar connection surfaces. These changes have led to a significant reduction in the stiffness of the system, making it more realistic and plausible. Following the same reasoning, the inner and outer rings were modified. Specifically, one quarter of the inner ring was reduced in size, while one quarter of the outer ring was enlarged. This created a clearance situation affecting one quarter of the vanes. Once again, only one quarter of the surface was selected to create a realistic distortion.

# Chapter 4

## Results

### 4.1 Reliability of the models

By creating and simulating a model, an attempt is made to study and predict the behaviour of its real counterpart. During this process, a series of simplifications are implemented, due both to the limits of representation of the real object and to the simulation tools. These simplifications inevitably reduce the reliability of the simulations and their results. For this reason, an attempt is made to keep the level of detail as high as possible and to limit the operations that could negatively affect accuracy. Some of these cannot be avoided, in particular:

- geometrical simplifications: it is not always possible to use the exact geometry of the model; in some cases, specific details are modified. These details might require an excessively small mesh to be accurately represented, even when they are not strictly necessary for the solution.
- limits of the analysis method:
  - discretization: a key step in finite element theory, as mentioned in Chapter 1.1, is the division of the continuous domain into a series of sub-elements. This division is fundamental to being able to solve the equations of the system but also inevitably introduces errors. These concern the loss of continuity of the system and the consequent introduction of a residual error. This is limited as the number of mesh elements increases.

- mesh: the size of the mesh plays a crucial role in simulations. A smaller mesh provides a better representation of the component's details, resulting in a more accurate solution. However, reducing the mesh size also significantly increases the required computation time. Therefore, a compromise must be found, as it is not possible to reduce the mesh size to zero nor to have a poor representation of the geometry of the system .
- assumption: to modify the contact surface profiles, it was necessary to assume certain deformation values, as written in Chapter 3, which may not necessarily correspond to the actual deformation of the components once they are realized. This introduces an additional level of approximation to the model.

For these reasons the validity and accuracy of the results cannot be physically assessed, as the actual system has not yet been built. In fact, testing the system once constructed would be necessary to verify the validity of certain assumptions and to evaluate the impact of the simplifications introduced.

## 4.2 Original model

As shown in Chapter 2, several models were created with increasing complexity, starting from the simplest one, which included only the substructures, to the most complex model, complete with all components.

The gradual introduction of the various components into the system has led to a stabilization of the first ten mode frequency values, which fall within the range of  $91.15 \text{ Hz}$  to  $156.04 \text{ Hz}$ .

Table 4.1 Results of the model with all the components

<b>Modes</b>	<b>Frequencies [Hz]</b>
<b>3</b>	91.15
<b>4</b>	115.69
<b>5</b>	117.45
<b>6</b>	118.69
<b>7</b>	119.41
<b>8</b>	124.74
<b>9</b>	133.47
<b>10</b>	154.75
<b>11</b>	155.86
<b>12</b>	156.04

Specifically, the inclusion of the shafts introduced two vibration modes, which can be attributed to the rigid-body motions of translation and rotation of the shafts themselves. These modes correspond to frequency values of 0 *Hz* and 0,268 *Hz*, so they are considered effectively zero. As a result, the first ten relevant modes correspond to modes three through twelve, which are listed in the table 4.1.

### 4.3 Motor's contact

Once the base model, complete with all components, was defined, the work on contact conditions began, starting with the interface between the motor and the hub body. As described in Chapter 2, each quarter of the motor surface was paired with each quarter of the rib surface of the hub body to evaluate all possible coupling scenarios, there are 9 of them:

1. quarter of the motor with no deformation paired with the quarter of the hub rib with maximum deformation
2. quarter of the motor with the small deformation paired with the quarter of the hub rib with the small deformation
3. quarter of the motor with the maximum deformation paired with the quarter of the hub rib with no deformation

4. quarter of the motor with small deformation paired with the quarter of the hub rib with the maximum deformation
5. quarter of the motor with no deformation paired with the quarter of the hub rib with the small deformation
6. quarter of the motor with small deformation paired with the quarter of the hub rib with no deformation
7. quarter of the motor with maximum deformation paired with the quarter of the hub rib with the small deformation
8. quarter of the motor with no deformation paired with the quarter of the hub rib with no deformation
9. quarter of the motor with the maximum deformation paired with the quarter of the hub rib with maximum deformation

They are presented in the table 4.2.

Table 4.2 Results of the different contact version of the motor

Modes	Frequencies [Hz] of the versions								
	1	2	3	4	5	6	7	8	9
<b>3</b>	91.14	91.10	91.10	91.10	91.10	91.10	91.10	91.08	91.08
<b>4</b>	115.69	115.82	115.82	115.82	115.82	115.82	115.82	115.76	115.76
<b>5</b>	117.45	117.41	117.41	117.41	117.41	117.41	117.41	117.42	117.42
<b>6</b>	118.69	118.55	118.55	118.55	118.55	118.55	118.55	118.55	118.55
<b>7</b>	119.41	119.26	119.26	119.26	119.26	119.26	119.26	119.27	119.27
<b>8</b>	124.31	124.37	124.43	124.41	124.41	124.36	124.36	124.40	124.35
<b>9</b>	133.47	133.58	133.59	133.58	133.58	133.58	133.58	133.44	133.44
<b>10</b>	154.43	154.36	154.36	154.35	154.35	154.35	154.36	154.35	154.35
<b>11</b>	155.84	155.83	155.84	155.84	155.83	155.84	155.83	155.83	155.83
<b>12</b>	156.04	156.03	156.03	156.03	156.03	156.03	156.03	156.03	156.03

Since each surface was divided into four parts, but two of them share the same radius, the total number of combinations was nine. The results are presented below. As can be observed, the worst-case scenario is combination number 9, where the

deformations are at their maximum in both the motor and the rib of the hub body, while the version with the highest frequencies is the first one, where the non-deformed surface quarters are in contact. This specific configuration was deliberately chosen for the subsequent tests. The goal was to analyse the system under the most extreme conditions, ensuring that the results would be as conservative as possible.

## 4.4 Bearing housing's contact

As mentioned in the previous chapters, the modifications were applied progressively, with each step building upon the previous ones. In this specific case, adjustments to the bearing housing contact profile were introduced in a model in which the motor profile had already been modified. This approach allowed for a systematic evaluation of how each change influenced the overall behaviour of the system. Following the same methodology used for the motor profile, all possible contact combinations between the various sections of the bearing housing surface and the corresponding sections of the hub body rib were carefully analysed. The results of these analyses are presented below in the table 4.3.

Table 4.3 Results of the implementation of different contact version of the bearing housing

Modes	Frequencies [Hz] of the versions								
	1	2	3	4	5	6	7	8	9
3	91.08	91.08	91.08	91.08	91.08	91.08	91.08	91.08	91.08
4	115.76	115.76	115.76	115.76	115.76	115.76	115.76	115.76	115.76
5	117.42	117.42	117.42	117.42	117.42	117.42	117.42	117.42	117.42
6	118.55	118.55	118.55	118.55	118.55	118.55	118.55	118.55	118.55
7	119.27	119.27	119.27	119.27	119.27	119.27	119.27	119.27	119.27
8	124.33	124.32	124.31	124.31	124.32	124.33	124.31	124.33	124.31
9	133.44	133.44	133.44	133.44	133.44	133.44	133.44	133.44	133.44
10	154.33	154.32	154.32	154.32	154.32	154.33	154.32	154.33	154.32
11	155.83	155.83	155.83	155.83	155.83	155.83	155.83	155.83	155.83
12	156.03	156.03	156.03	156.03	156.03	156.03	156.03	156.03	156.03

It can be observed that the differences in the results are generally minimal, as most versions exhibit identical frequency values. However, there are a few exceptions,

specifically in mode number 8 and mode number 10, where slight variations appear in certain cases. One notable example is version 9, which shows small deviations.

As previously seen with the motor, this particular version corresponds to the configuration in which the quarters of the contact surface experience the greatest deformation compared to the baseline model. This suggests that, while most configurations yield consistent results, the specific contact conditions in certain cases can introduce slight changes in the system's dynamic behaviour.

## 4.5 Flanged side's contact

The next modification, following those previously discussed, involves the flanges of both the motor and the bearing housing. As mentioned in Chapter 3 and shown in Fig. 3.5 and 3.10, a series of surfaces were specifically created around each flange hole. This adjustment was made to replicate the connection as accurately as possible. As a result, this modification introduced a change in the overall stiffness of the connection.

Unlike the previous modifications, for which multiple versions were analysed, this particular change did not require the creation of different variations. Instead, a single model was developed, incorporating all the modifications introduced up to this point.

Table 4.4 Results of the implementation of the flanged side's contact

<b>Modes</b>	<b>Frequencies [Hz]</b>
<b>3</b>	91.06
<b>4</b>	115.76
<b>5</b>	117.42
<b>6</b>	118.55
<b>7</b>	119.27
<b>8</b>	124.23
<b>9</b>	133.43
<b>10</b>	154.29
<b>11</b>	155.83
<b>12</b>	156.03

Once again, the values presented in the table 4.4 show only minor differences compared to those found in the previous analyses. For the majority of vibration modes, the frequencies remain unchanged, indicating that the modifications introduced have had little to no impact on the system's overall dynamic behaviour. However, there are two exceptions: modes 8 and 10, which exhibit slight variations in their frequency values, although these differences are relatively small. Mode 8, in this case, corresponds to a lateral bending mode, as illustrated in the figure 4.1.

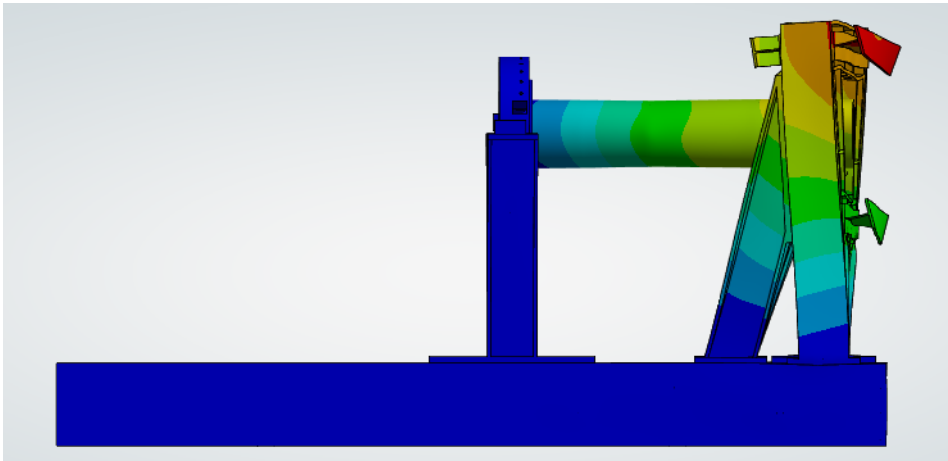


Fig. 4.1 Lateral view of mode 8

## 4.6 Vanes contacts

The next modification, implemented after the adjustment to the flange holes, focused on improving the representation of the vanes. In particular, the contact interactions between individual vanes and between the vanes and its carrier were refined. This improvement allowed for a more accurate definition of the stiffness of the entire component, ensuring that the model better reflects realistic behaviour. By enhancing these contacts, the structural response of the system became more representative of actual operating conditions. As with the previous modification, it was not necessary to create multiple versions of the model. The adjustments made were directly integrated into the existing model.

With this modification, the results have changed noticeably, particularly for modes 8 to 11, as shown in table 4.5. In these specific cases, the difference compared to the previous model exceeds a value of  $1 \text{ Hz}$ , highlighting the significant influence

of the changes introduced. This suggests that the refinement of the vane contacts has had a direct impact on the system's dynamic behaviour. For the remaining modes, the frequency values remain largely consistent with those of the previous model, showing only minor deviations.

Table 4.5 Results of the implementation of the vanes contacts

Modes	Frequencies [Hz]
3	90.98
4	115.82
5	117.40
6	118.54
7	119.26
8	123.23
9	132.20
10	153.49
11	154.64
12	156.05

Among the affected modes, mode 9 exhibits the most pronounced variation, standing out as the one most influenced by the modification. It corresponds to a torsional mode primarily affecting the vanes. The fact that it is mainly driven by the torsion along the central axis of the system explains its significant impact on the results and the deviation from the previous model, as illustrated here.

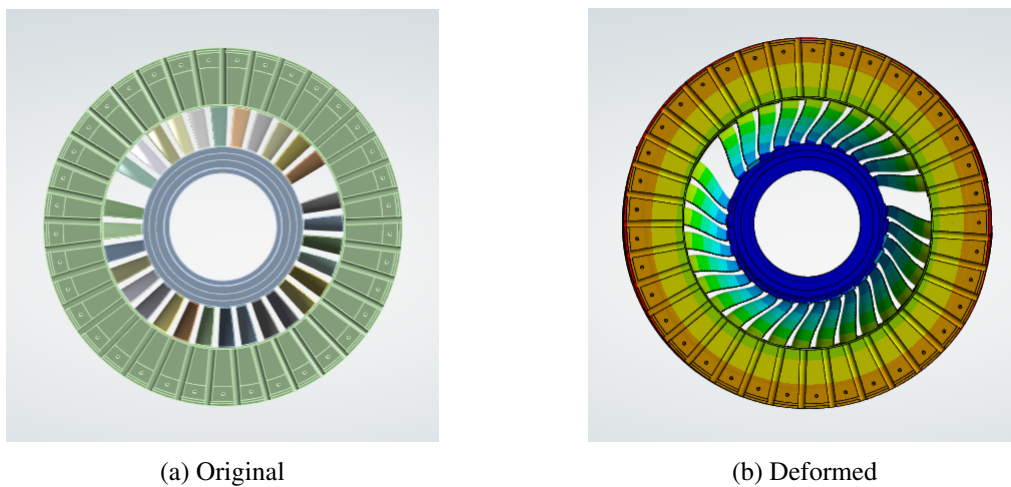


Fig. 4.2 Front view of the vanes on mode 9

## 4.7 Flatness modification

As stated in Chapter 3, the last modification made to the system concerned the flatness of the flanged surfaces. Specifically, the surfaces of both the bearing housing and the motor were adjusted so that one-quarter of each surface was positioned on a slightly different plane than the remaining three quarters. This change aimed to better simulate potential geometric imperfections that could occur in the real assembly.

This modification was integrated into the model developed so far, meaning that the final version now includes all previous refinements. These include the adjustments to the contact surfaces of the bearing housing and motor, the modifications to the flange holes of these components, and the improved definition of the vane contacts. By incorporating all these changes, the model provides a more detailed and realistic representation of the expected behaviour of the system.

Table 4.6 Results of the implementation of the flatness modification

<b>Modes</b>	<b>Frequencies [Hz]</b>
<b>3</b>	90.93
<b>4</b>	115.82
<b>5</b>	117.39
<b>6</b>	118.54
<b>7</b>	119.26
<b>8</b>	123.23
<b>9</b>	131.58
<b>10</b>	153.44
<b>11</b>	154.59
<b>12</b>	156.03

The results shown in the table 4.6 remain fairly consistent across most modes, with noticeable differences appearing only in mode 9. This variation is understandable, as the modified flange surfaces are positioned perpendicularly to the axis that governs the torsional movement in mode nine. Since these surfaces play a crucial role in the structural response of the system, their altered flatness directly affects the stiffness and dynamic behaviour in this specific mode, leading to the observed deviations in frequency values.

## 4.8 Graphs and modes details

Based on the analyses conducted so far, it is now possible to determine the overall differences between all the models that have been created throughout the study. By comparing their results in the table 4.7, it becomes evident which specific vibration modes have experienced the most significant reductions in frequency. Additionally, this comparison allows for a precise quantification of these decreases, providing a clearer understanding of how each modification has influenced the dynamic behaviour of the system.

Table 4.7 Results of every model created

Mode	Frequencies [Hz]					
	Original	Motor	B. housing	Flanges	Vanes	Flatness
<b>3</b>	91.15	91.08	91.08	91.06	90.98	90.93
<b>4</b>	115.69	115.76	115.76	115.76	115.82	115.82
<b>5</b>	117.45	117.42	117.42	117.42	117.40	117.39
<b>6</b>	118.69	118.55	118.55	118.55	118.54	118.54
<b>7</b>	119.41	119.27	119.27	119.27	119.26	119.26
<b>8</b>	124.74	124.35	124.31	124.23	123.23	123.23
<b>9</b>	133.47	133.44	133.44	133.43	132.20	131.58
<b>10</b>	154.75	154.35	154.32	154.29	153.49	153.44
<b>11</b>	155.86	155.83	155.83	155.83	154.64	154.59
<b>12</b>	156.04	156.03	156.03	156.03	156.05	156.03

In the table 4.7, each column presents the frequencies of the complete model, progressively incorporating all the modifications introduced in the preceding columns. For example, the column 'Vanes' represents the results of the model that includes not only the modifications made to the vanes, but also those applied to the flanges, bearing housing, and motor. This explains why the frequency values systematically decrease as we move from left to right, starting from the original model and progressing through each successive modification until reaching the most altered version.

To better visualize the overall impact of these changes, the table 4.8 provides a summary of the cumulative differences between the various models, allowing for a

clearer understanding of how much the frequencies deviate from those of the initial configuration.

Table 4.8 Variation of each version compared to the original model

Mode	Delta [Hz]				
	Motor	B. housing	Flanges	Vanes	Flatness
<b>3</b>	-0.06	-0.06	-0.09	-0.16	-0.22
<b>4</b>	0.07	0.07	0.07	0.13	0.13
<b>5</b>	-0.03	-0.03	-0.03	-0.05	-0.06
<b>6</b>	-0.14	-0.14	-0.14	-0.15	-0.15
<b>7</b>	-0.14	-0.14	-0.14	-0.15	-0.15
<b>8</b>	-0.39	-0.43	-0.51	-1.51	-1.51
<b>9</b>	-0.03	-0.03	-0.04	-1.27	-1.89
<b>10</b>	-0.40	-0.43	-0.46	-1.26	-1.31
<b>11</b>	-0.03	-0.03	-0.03	-1.22	-1.27
<b>12</b>	-0.01	-0.01	-0.01	0.01	-0.01

The first significant mode, number 3, appears at a frequency that remains relatively stable across all modifications and consistently exceeds 90 Hz. This mode is characterized by the highest energy involvement, making it the primary mode of the system. However, despite its importance from a structural point of view, it does not play a crucial role in the context of this analysis. This is because the test rig is designed to operate at much lower frequencies, which means that mode 3 will never be excited during normal working conditions. Mode 3 corresponds to a bending mode and is illustrated in Figure 4.3.

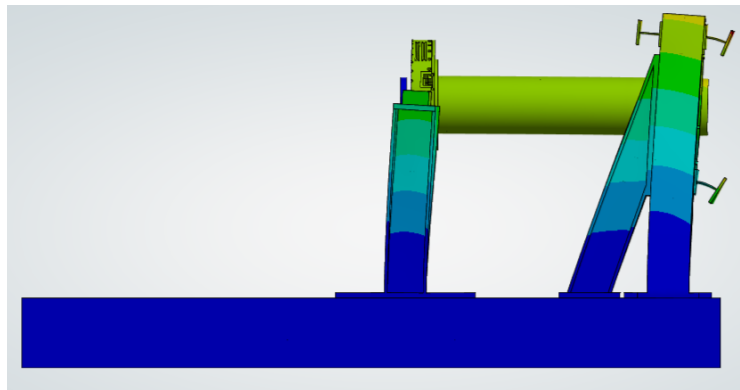


Fig. 4.3 Lateral view of mode 3

Therefore, the analysis concentrated on evaluating the effects of the modifications on each mode, even though they are not as significant as the primary one.

It can be observed that mode 4 presents a unique trend, as its frequency slightly increases with the progressive modifications. However, this particular mode primarily involves only specific sections of one of the two substructures. For better clarity, it is illustrated in the figure 4.4.

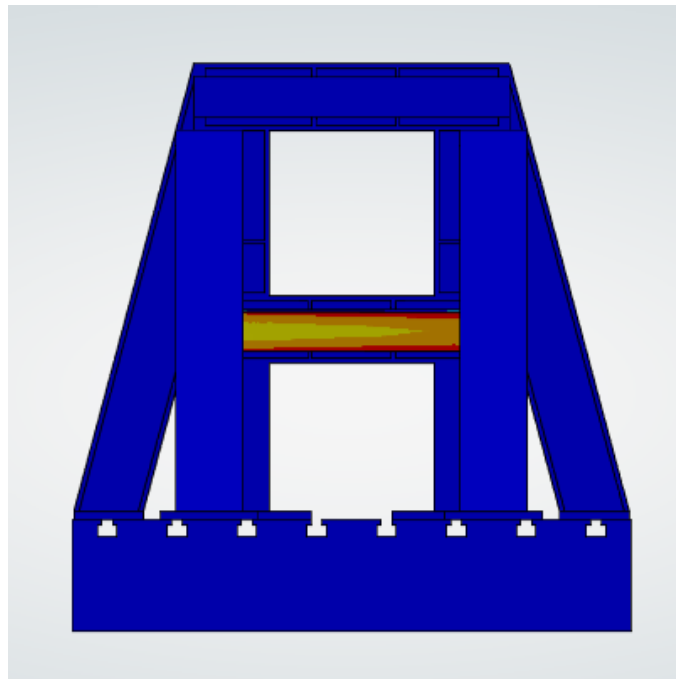


Fig. 4.4 Mode 4

The modes from 8 to 11 are the most affected by the modifications introduced, showing the largest deviations compared to the original model. These differences are significantly more pronounced than those seen in the other modes, confirming their higher sensitivity to changes in the system.

Specifically, the following table 4.9 highlights which modification had the greatest impact by showing the relative percentage decrease in frequency for each modification introduced. This allows for a clearer understanding of how each individual change contributed to the overall variation in the system's dynamic behaviour.

Table 4.9 Percentage difference between models

Mode	Delta % [Hz]				
	Motor	B. housing	Flanges	Vanes	Flatness
<b>8</b>	-0.31%	-0.03%	-0.06%	-0.80%	0.00%
<b>9</b>	-0.02%	0.00%	-0.01%	-0.92%	-0.47%
<b>10</b>	-0.26%	-0.02%	-0.02%	-0.52%	-0.03%
<b>11</b>	-0.02%	0.00%	0.00%	-0.76%	-0.03%

Or, illustrated by graphs:

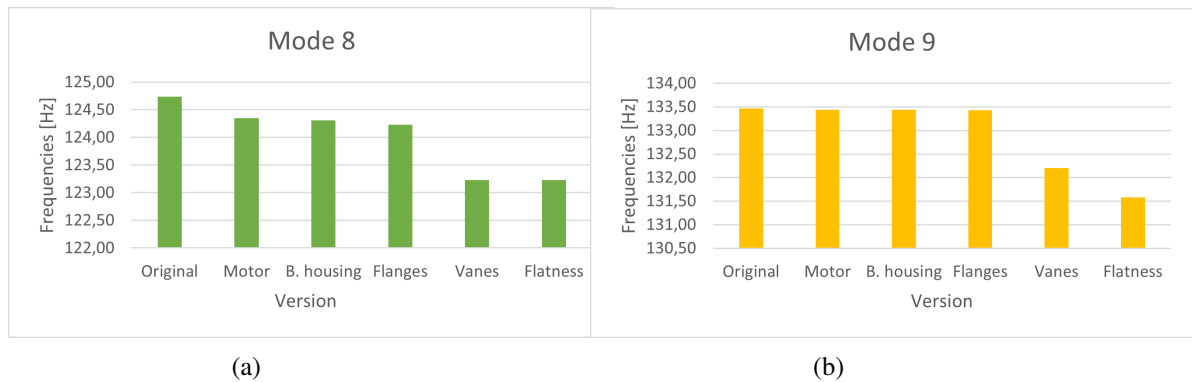


Fig. 4.5 Frequency graphs of modes 8 (a) and 9 (b)

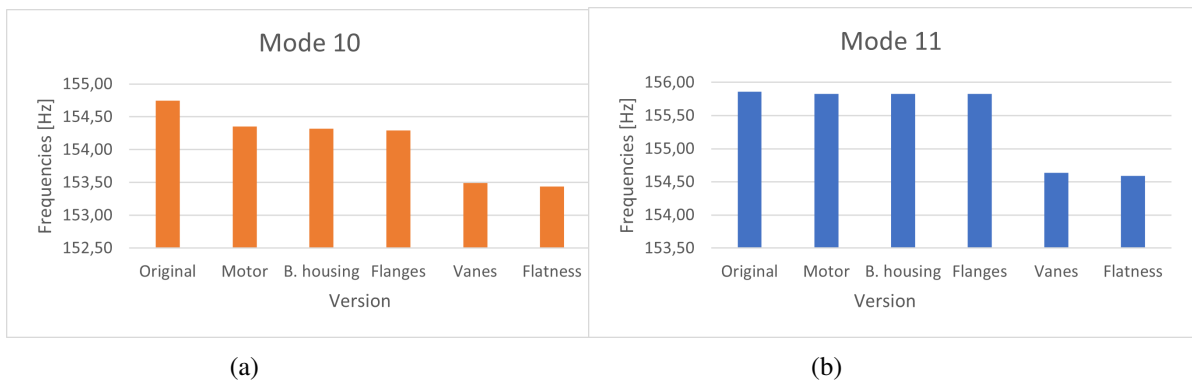


Fig. 4.6 Frequency graphs of modes 10 (a) and 11 (b)

The last two modifications turned out to be the most significant in influencing the system's behaviour. Specifically, the adjustment of the flatness had a noticeable effect on mode 9, while the modification of the vanes' contacts significantly impacted modes 8 through 11. Among these, the latter modification proved to be the most influential, especially for mode 9, which, as shown in Fig.4.2b, exhibits a particularly strong interaction with the vanes. However, the influence extends beyond just mode 9, modes 8, 10, and 11 also show considerable variation, indicating that the way the vanes make contact plays a fundamental role in the overall dynamic response of the system. Modes 8 and 9 were previously presented in Figures 4.1 and 4.2b, respectively, while modes 10 and 11, which mainly involve the two substructures, are illustrated below in the figure 4.7.

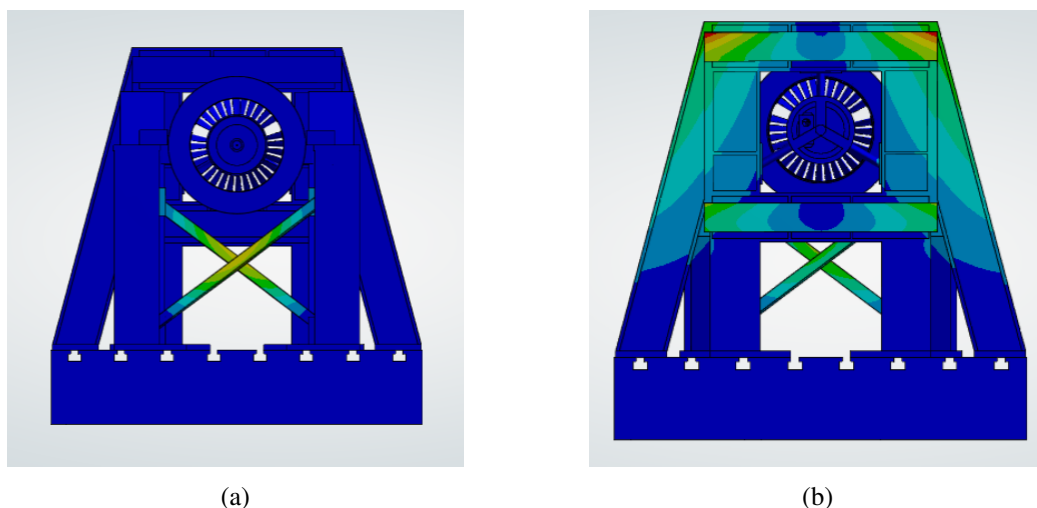


Fig. 4.7 Mode 10 (a) and mode 11 (b)

# Chapter 5

## Conclusion

The primary objective of this study was to analyse the dynamic behaviour of the new test section of the acoustic wind tunnel, with a focus on understanding the effects of contact modifications on the overall dynamic response of the system. The initial expectation was that, given the inherently stiff structure and contacts, the changes in modal frequencies would be minimal across successive modifications.

The analysis revealed that the variations in modal frequencies from one version to the next are generally very small, often less than 1 percentage point. This observation supports the notion that both the stiffness of the contact interfaces and the rigidity of the surrounding structure play dominant roles in governing the system's dynamic behaviour. Two main hypotheses can be drawn from these results. First, the contact interfaces, even after modification, might remain too stiff to produce significant reductions in the modal frequencies. Second, the overall structural stiffness of the test section might overshadow the effects of localized contact modifications. Only mode 9, associated with the torsion of the vanes system and its carrier, shows slightly more pronounced changes, suggesting that localized phenomena might be more sensitive to the modifications applied. For future investigations, it would be valuable to conduct experimental validations, which could help clarify whether the observed minimal frequency changes are due to the stiffness of the contacts or the surrounding structure.

In summary, the study confirms that the new test section maintains a high level of stiffness and provides a solid foundation for understanding the dynamic behaviour

of the test section and highlights key areas for future research, thus enhancing the design and performance of such complex system.

# References

- [1] Leibniz Universitat Hannover. Aeroacoustic Wind Tunnel. <https://www.tfd.uni-hannover.de/en/research/our-services/test-rigs/aeroacoustic-wind-tunnel/>, 2022. [Online; accessed 2024].
- [2] Giancarlo Genta. *Vibration Dynamics and Control*. Springer, 2009.
- [3] R + W the coupling. BK6. <https://www.rw-couplings.com/product/bk6/>. [Online; accessed 2024].
- [4] Manner. XtremaHP. <https://www.sensortelemetrie.de/en/products/torque-measurement-technology/xtrema-torque-the-highly-accurate-measuring-flange-series/>. [Online; accessed 2024].

# **Appendix A**

## **Datasheet**

### **A.1 BK6**

# BK6

## Steckbar, mit Konusklemmring

15 – 1.500 Nm



### Eigenschaften

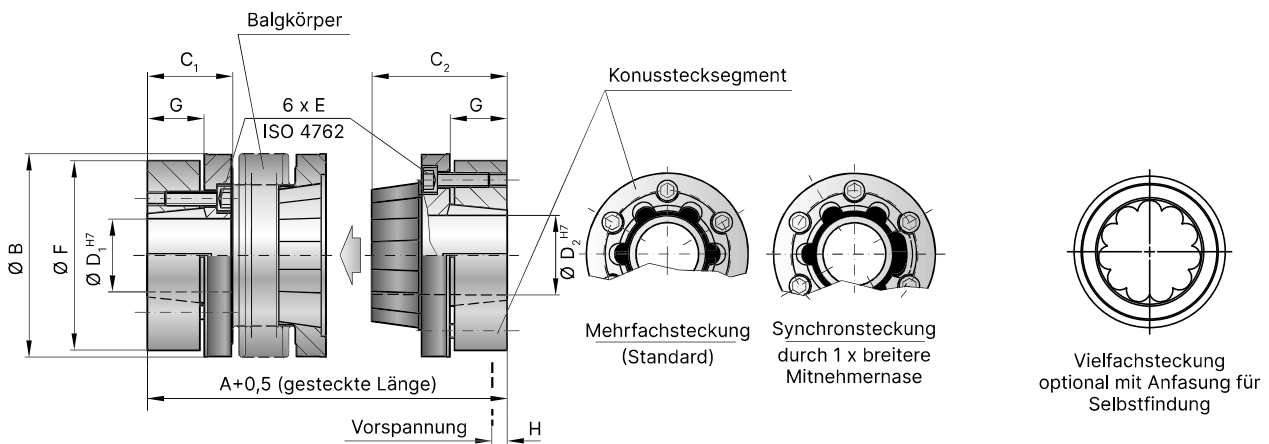
- Axial montierbar
- einfache Montage & Demontage
- Elektrisch und thermisch isolierend
- Absolut spielfrei & verdrehsteif

### Material

- **Balg** aus hochelastischem Edelstahl
- **Naben** aus Stahl
- **Konussegment** aus hochfestem Kunststoff

### Design

Zwei Konusklemmringnaben mit je sechs Schrauben und Abdrückschrauben, davon eine Konusklemmringnabe mit konischer Steckverbindung. Kurzzeitig 1,5-facher Wert von  $T_{KN}$  zulässig.



## Modell BK6

Serie			15	30	60	150	300	500	800	1.500
Nenn Drehmoment (Nm)	$T_{KN}$		15	30	60	150	300	500	800	1.500
Kupplungslänge (gesteckt) (mm)	$A^{+0,5}$		58 65	68 76	79 89	97 109	113 127	132 145	140 158	157
Außendurchmesser (mm)	B		49	55	66	81	110	124	133	157
Passungslänge (mm)	$C_1$		13,3	21,5	17,5	30	37	32	42,5	53
Passungslänge (mm)	$C_2$		29	34	39	49,5	59	68	74	90,5
Bohrungsdurchmesser möglich von Ø bis Ø H7 (mm)	$D_{1/2}$		10-22	12-24	12-32	15-40	24-56	30-60	40-62	50-75
Befestigungsschrauben ISO 4762	E		M4	M5	M5	M6	M8	M8	M10	M12
Anzugsmoment (Nm)			3,5	6,5	8	12	30	32	55	110
Klemmringdurchmesser (mm)	F		46,5	51	60	74	102	114	126	146
Konuslänge (mm)	G		9,5	10,5	11,5	17,5	20	23	27	32
Axiale Vorspannung ca. (mm)			0,2 - 1,0	0,5 - 1,0	0,5 - 1,5	0,5 - 1,5	0,5 - 1,5	1,0 - 2,0	1,0 - 2,0	0,5 - 1,5
Rückstellkraft bei max. Vorspannung (N)	H		20 12	50 30	70 45	82 52	157 106	140 96	400	650
Trägheitsmoment ( $10^{-3}$ kgm <sup>2</sup> )	$J_{ges}$		0,1 0,12	0,2 0,25	0,4 0,45	2,0 2,5	5,4 6,1	8,4 9,1	17,5	44
Masse ca. (kg)			0,3 0,32	0,5 0,52	0,82 0,84	1,6 1,7	4,1 4,2	6,0 6,3	8,1	16,2
Torsionssteife ( $10^3$ Nm/rad)	$C_T$		10 8	20 14	38 28	88 55	225 175	255 245	400	660
Axial* ± (mm)			0,5 1	0,5 1	0,5 1	1 2	1,5 2	2,5 3,5	3	2
Lateral ± (mm)		max. Werte	0,15 0,2	0,2 0,25	0,2 0,25	0,2 0,25	0,25 0,3	0,3 0,35	0,35	0,35
Angular ± (Grad)			1 1,5	1 1,5	1 1,5	1 1,5	1 1,5	1 1,5	1,5	1,5
Lateralfedersteife (N/mm)	$C_r$		475 137	900 270	1.200 420	1.550 435	3.750 1.050	2.500 840	2.000	3.600

\* zusätzlich nach max. Vorspannung. Höhere Drehmomente auf Anfrage

## A.2 XTreMA

## torque measuring flange

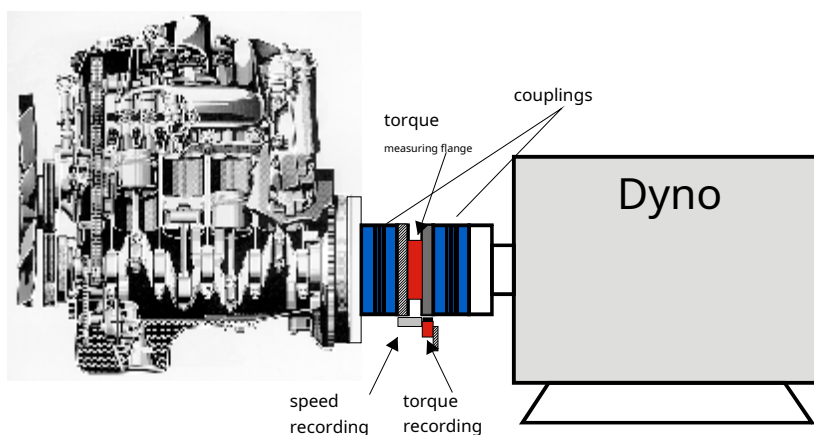
**Improved zero point drift  $T_k \leq 0.005\%/10^\circ\text{C}$**

**Improved  $T_{kc}$  behavior  $0.005\%/10^\circ\text{C}$**



### Characteristic features:

- ✓ Nominal torques:  
50 N m, 100 N m, 200 N m, 500 N m, 1 kN m, 2 kN m, 3 kN m, 5 kN m, 10 kN m
- ✓ rated speeds of 10000min<sup>-1</sup> up to 25000min<sup>-1</sup> (depending on the measuring range)
- ✓ Accuracy class: 0.02 (optional 0.02)
- ✓ Measuring frequency range up to 1 kHz (optional 10 kHz (-3dB))
- ✓ Low rotor weights and moments of inertia
- ✓ Digital transmission of measured values
- ✓ Short design, compatible flange pattern to HBM (DIN flange pattern)
- ✓ Temperature range -40..160°C (optional)
- ✓ Integrated speed measurement (high resolution)



integrated pick-up

- frequency (10+/-5kHz)
- Voltage (U) +/10V
- current (I) 4..20mA
- Remote Control
- energy
- Remote Shunt on/off

## topologies



- energy
- Remote Shunt on/off
- torque (digital)
- temperature (digital)
- status
- Remote Control

max. distance: 100 m

flange with offset pick up



- Ethernet (digital)
- EtherCat (digital)
- USB (digital)
- frequency (10+/-5kHz)
- Voltage (U) +/10V
- current (I) 4..20mA
- Remote Control
- energy
- Remote Shunt on/off

evaluation unit

# Technical data

torque measuring system										
type		- HP								
accuracy class		0.02								
nominal torque $M_{nom}$	kNm	0.05	0.1	0.2	0.5	1	2	3	5	10
nominal value (Range between torque = zero and nominal torque)										
voltage output 10 V	V	+/-10								
frequency output 60 kHz	kHz	+/-30								
Digital output EtherCat 16 bit	digital value	+/-29491 (471859 <sub>3</sub> )								
Digital output EtherNet TCP/IP 16 bit	digital value	+/-29491 (471859 <sub>3</sub> )								
Digital Output CAN 16 Bit	digital value	+/-29491 (471859 <sub>3</sub> )								
characteristic tolerance (Deviation of the initial value at M .....of the characteristic value)	%	0.05 (0.01 <sup>1)</sup> )								
Output signal at torque = zero										
voltage output	V	0								
frequency output 60 kHz	kHz	60								
Digital output	digital value	32768 (524288 <sup>3)</sup> )								
nominal output signal										
voltage output										
at positive nominal torque	V	+ 10								
at negative nominal torque	V	- 10								
frequency output 60 kHz <sup>7)</sup>										
at positive nominal torque	kHz	90 (5V TTL 0/5V) (15 <sup>7)</sup> )								
at negative nominal torque	kHz	30 (5V TTL 0/5V) (5 <sup>7)</sup> )								
Digital output										
at positive nominal torque	digital value	62258 (996147 <sup>3)</sup> )								
at negative nominal torque	digital value	3278 (52429 <sup>3)</sup> )								
load resistance										
voltage output	kOhm	> 2								
frequency output 60 kHz	kOhm	> 10								
long-term drift over 48 hours										
voltage output	%	<+/-0.03								
frequency output 60 kHz	%	<+/-0.03								
measuring frequency range (-3 dB)	kHz	1 ( 2 <sup>4)</sup> , 5 <sup>5)</sup> , 10 <sup>6)</sup> )								
group runtime	us	<400 (<250 <sup>4)</sup> , <130 <sup>5)</sup> , <40 <sup>6)</sup> )								
residual ripple(voltage output)	mV	<10								
Temperature influence per 10 K in the nominal temperature range on the output signal, relative to the actual value of the signal span										
frequency output	%	+/- 0.02								
digital output	%	+/- 0.02								
voltage output	%	+/- 0.05								
to the zero signal, relative to the zero characteristic value										
frequency output	%	+/- 0.01 (+/-0.005 <sub>2</sub> )								
digital output	%	+/- 0.01 (+/-0.005 <sub>2</sub> )								
voltage output	%	+/- 0.04 (+/-0.02 <sub>2</sub> )								
max. dynamic range										
frequency output 60 kHz	kHz	+/-31.62 (+/-5.27 <sub>7</sub> )								
digital output	digits	+/-32768 (524288 <sub>3</sub> )								
voltage output	V	+/-11.2								
energy supply										
nominal supply (protective extra-low voltage DC)	V	+ 20..28V								
current consumption during measurement	A	< 0.7								
current consumption during start-up operation	A	< 1A								
rated input power	W	< 5								
max. cable length	m	100								

1) Option improved parameter tolerance  
 2) Zerodrift option  
 3) Option signal resolution 20 bit  
 4) Option measuring signal bandwidth 2 kHz

5) Option measuring signal bandwidth 5 kHz  
 6) Option measuring signal bandwidth 10 kHz  
 7) Frequency output option 10 kHz+/-5 kHz

## Technical data (continued 1)

nominal torque M <sub>nom</sub>	kNm	0.05	0.1	0.2	0.5	1	2	3	5	10	
<b>Linearity deviation including hysteresis,</b> based on the nominal value											
voltage output 10 V	%	< +/- 0.02									
frequency output 60 kHz	%	< +/- 0.02									
Digital output	%	< +/- 0.02									
Rel. Standard Deviation of Repeatability according to DIN 1319 based on output signal change		< +/- 0.005									
shunt signal Tolerance of the shunt signal, relative to M <sub>nom</sub>		about 80% of M <sub>nom</sub> < +/- 0.02									
Shunt signal, relative to M <sub>nom</sub>	%	80									
max. voltage shunt signal	%	12									
shunt signal on (active low)	V	< 1 (GND)									
shunt signal off	V	> 2.5									
Total accuracy related to nominal torque M <sub>nom</sub> based on 10 K temperature change (digital output)											
60..100% of M <sub>nom</sub>	%	< ±0.007									
20..60% of M <sub>nom</sub>	%	< ±0.005									
0..20% of M <sub>nom</sub>	%	< ±0.003									
<b>General Information</b>											
EMC emission (according to EN 61326-1, section 7) <small>radio interference field strength</small>	-	Class B									
Immunity (EN 61326-1, Table 2)											
electromagnetic field	V/m	80									
Magnetic field	A/m	200									
<b>Electrostatic discharges (ES)</b>											
contact discharge	kV	20									
air discharge	kV	10									
Fast transients (bursts)	kV	1									
surge voltage	kV	1									
Line-based interference	V	10									
protection class according to EN 60529 standard		Ip54 (IP67 <sup>2)</sup> )									
Weight <small>approx. rotor</small> <small>approx. stator</small>	kg kg	0.9	0.9	1.0	2.0	2.1	4.0	4.1	6.1	10.2	
reference temperature	°C	23									
operating temperature range	°C	- 10..+70									
Extended temperature range <sup>9)</sup>	°C	- 40..+160									
storage temperature range	°C	- 50..+160									
<b>Mechanical shock resistance according to EN 60068-2-27</b>											
Number	n	100									
<small>Length of time</small>	ms	3									
acceleration (half sine)	m/s <sup>2</sup>	650									
<b>Vibration stress in 3 directions after EN 60068-2-27</b>											
frequency range	Hz	10...2000									
<small>Length of time</small>	h	2.5									
acceleration (amplitude)	m/s <sup>2</sup>	200									
rated speed	min <sup>-1</sup>	20,000			20,000		15,000		12,000		10,000
Option increased nominal torsional strength	min <sup>-1</sup>	32,000			25,000		18,000		15,000		15,000
<b>load limits <sup>11)</sup></b>											
limit torque related to M <sub>nom</sub>	%	400									
Fracture torque related to M <sub>nom</sub>	%	800									
limit longitudinal force <sup>11)</sup>	kN	5	5	10	20	29	45	53	90	120	
limit shear force <sup>11)</sup>	kN	1	1	2	6	8	15	17	20	24	
limit bending moment <sup>11)</sup>	kNm	0.03	0.03	0.1	0.3	0.36	0.8	0.9	1.2	1.7	
Vibration range according to DIN 50100 (peak/peak) <sup>12)</sup>	kNm	0.20	0.20	0.40	1.0	2.0	4.0	5.1	8.5	1.7	

8) Option protection class IP67

9) Option extended operating temperature range

10) Option increased speed stability

11) Static and dynamic

12) The nominal torque must not be exceeded

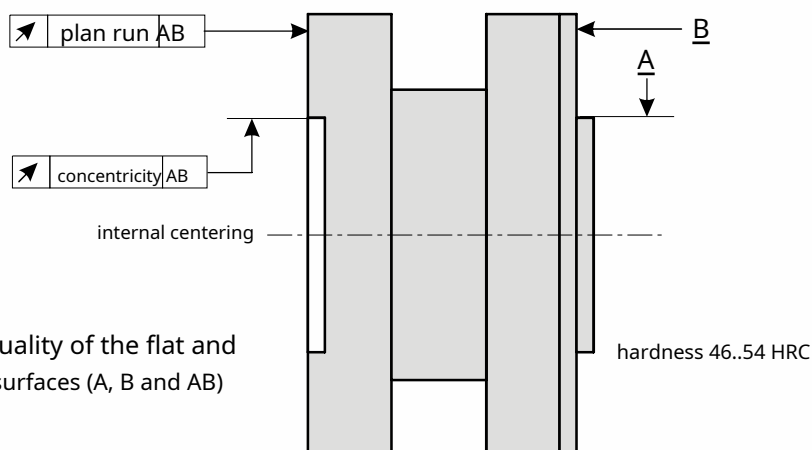
## Technical data (continued 2)

nominal torque $M_{nom}$	kNm	0.05	0.1	0.2	0.5	1	2	3	5	10
Influence of the measured value by parasitic forces <sup>14)</sup>										
Crosstalk factor bending moment $M_B$	kN m/kN m	< 0.002								
crosstalk factor lateral force $F_s$	kN m/kN	< 0.0002								
crosstalk factor axial force $F_z$	kN m/kN	< 0.00015								
<b>Mechanical values</b>										
torsional stiffness $c_T$	kN m/rad	79	79	149	561	895	2293	2865	4854	10989
angle of rotation at $M_{nom}$	degree	0.037	0.073	0.077	0.051	0.064	0.051	0.061	0.059	0.052
stiffness in axial direction $c_a$	kN/mm	125	125	167	437	587	939	1090	1040	1412
Stiffness in radial direction $c_r$	kN/mm	58	58	105	336	541	801	1028	985	1272
Stiffness at bending moment about radial axis $c_b$	kN m/degree	1.20	1.20	2.10	2.89	3.8	9.1	10.4	13.7	27.2
Maximum deflection at limit longitudinal force	mm	<0.09	<0.09	<0.09	<0.045	<0.04	<0.05	<0.06	<0.08	<0.09
Additionally max. concentricity error at limit transverse force	mm	<0.02								
Additional plane parallelism deviation at limit bending moment at $d_B$	mm	<0.07	<0.07	<0.07	<0.10	<0.085	<0.15	<0.18	<0.15	<0.12
balancing quality level according to DIN ISO 1940		G6.3								
Permissible maximum oscillation path of the rotor (peak-to-peak) <sup>13)</sup> Shaft vibration in the area of the connecting flanges in accordance with ISO 7919-3										
normal operation	um	$S_{(pp)} = \frac{9000}{\sqrt{n}}$ (n in $\text{min}^{-1}$ )								
Start and stop operation/resonance ranges (temporary)	um	$S_{(pp)} = \frac{13200}{\sqrt{n}}$ (n in $\text{min}^{-1}$ )								
<b>moment of inertia of the rotor</b>	kg m <sup>2</sup>	0.0016	0.0016	0.0017	0.0048	0.0050	0.0151	0.0152	0.0335	0.0859
axis of rotation (without taking the flange screws into account)										
<b>Max. permissible eccentricity</b>	mm	5								
rotor - stator										
<b>Max. permissible axial displacement of the rotor - stator</b>	mm	+ /-2								

13) Influence of the vibration measurements by concentricity errors, impact, form errors, notches, grooves, local residual magnetism must be separated from the actual shaft vibration

14) Basis: Application of only one parasitic force type at a time

### radial and axial runout tolerances



nominal torque $M_{nom}$	kN m	0.05	0.1	0.2	0.5	1	2	3	5	10
axial runout tolerance	mm	0.01	0.01	0.01	0.01	0.01	0.01	0.02	0.02	0.02
concentricity tolerance	mm	0.01	0.01	0.01	0.01	0.01	0.01	0.02	0.02	0.02
<b>Integrated speed measurement (inductive, IP67)</b>										
Inductive speed detection (track A/B)	DZ stamps /U	n/a	60				80	100	120	
pickup distance to the rotor	mm	0.8+/-0.4								
<b>Integrated speed detection (laser scanning, IP42)</b>										
Optical speed detection (track A)	DZ stamps /U	180			200	260	300	360		
Pick Up Distance to Rotor	mm	20+/-19								

13) Option accuracy class 0.02%